ABSTRACT

Title of thesis: NUMERICAL STUDIES OF STOKES FLOW IN CONFINED GEOMETRIES

Yechun Wang, Master of Science, 2004

Thesis directed by: Professor Panagiotis Dimitrakopoulos
Department of Chemical Engineering

The current thesis includes two distinct projects. The first study involves the development of a novel three-dimensional Spectral Boundary Element algorithm for interfacial dynamics in Stokes flow. Our algorithm is the only available high-order/high-accuracy methodology for the problem of droplet deformation in viscous flows. By applying this algorithm to several interfacial problems, we find that our results are in excellent agreement with experimental findings, analytical predictions and previous numerical computations.

The second project studies viscous flows over a protuberance on the inner wall of a solid microtube, a problem relevant to both physiological systems and microfluidic devices. The shear stress, drag and torque on the protuberance are determined as functions of the spreading angle and the relative size of the protuberance which may represent leukocytes, blood clots or endothelial cells on the microvessel wall. This study facilitates the understanding of mechano-transduction phenomena as well as cell adhesion in blood flow.

NUMERICAL STUDIES OF STOKES FLOW IN CONFINED GEOMETRIES

by

Yechun Wang

Thesis submitted to the Faculty of the Graduate School of the
University of Maryland, College Park in partial fulfillment
of the requirements for the degree of
Master of Science
2004

Advisory Committee:

Professor Panagiotis Dimitrakopoulos, Chair/Advisor
Professor Elias Balaras
Professor Timothy A. Barbari
Professor Sheryl H. Ehrman

Acknowledgements

I would like to thank all the people who have made this thesis possible.

First of all, I must thank my advisor, Professor Panagiotis Dimitrakopoulos, for his guidance in my research during these two years and for his tremendous help in my thesis preparation.

I thank all the members of our research group, Mr. Jingtao Wang, Ms. Inuka Dissanayake and Mr. Walter R. Dodson, for their helpful discussions. I am also thankful to the staff of the Chemical Engineering Department for their kind assistance.

I own my gratitude to my parents, Mr. Feng Wang and Mrs. Hui Yang, for their love and support from the other end of this planet.

This research was supported in part by the National Science Foundation (grant CTS-0218770), the Petroleum Research Fund of the American Chemical Society, and the National Center for Supercomputing Applications in Illinois.

Table of Contents

List of Tables

List of Figures

Chapter 1

Introduction

The current thesis considers two distinct projects: (a) the development of a novel Spectral Boundary Element algorithm for interfacial dynamics in Stokes flow, and (b) the physical problem of Stokes flow over a hump/cell attached to a microtube wall where for the first time a three-dimensional cylindrical model is employed.

1.1 Droplet deformation

A single droplet suspended in a host fluid deforms in response to an external flow. As long as the shear rate of the external flow is below some critical value, the deformation of the droplet reaches an equilibrium state. When the critical value in shear rate is exceeded, the droplet breaks up into two or more smaller droplets.

This physical phenomenon is one of the building bricks for large-scale simulations of multi-phase fluids such as foams and emulsions which have numerous applications including the tertiary oil recovery, environmental remediation, coating and condensation processes. It also acts as a prototype for the deformation and burst of artificial capsules and blood cells in micro-vessels which may give advice on the design of biomedical devices.

To facilitate the study of these systems, in the current thesis we develop a high-order/high-accuracy Spectral Boundary Element algorithm for interfacial dynamics in Stokes flow by combining our Spectral Boundary Element method for fixed surfaces with an explicit time-integration algorithm and a novel interfacial smoothing scheme. The main attraction of this approach is that it exploits all the benefits of the spectral methods (i.e., exponential convergence and numerical stability) and the versatility of the finite element method (i.e., the ability to handle the most complicated geometries). These properties result in a great computational efficiency which facilitates the study of a wide range of problems involving interfaces in Stokes flow.

1.2 Stokes flow over a hump in a microtube

Viscous flows over protuberances on the inner wall of solid tubes commonly appear in both physiological phenomena and microfluidic devices. In physiological systems, the protuberance may stand for leukocytes (white blood cells), blood clots, or separated endothelial cells adhering to the inner surface of capillaries or venules. The study of the shear stress exerted on the protuberance can facilitate the understanding of the mechano-transduction phenomena since the endothelial cells send out chemical signals in response to the hemodynamic shear force they received[14, 27]. The study of the fluid force on the protuberance is also important because biomechanical forces influence endothelial structure and function, such as the permeability to macromolecules, lipoprotein accumulation and the repair near branch points[27]. The study of the total drag and torque on the protuberance may also be helpful in

analyzing the leukocyte-endothelial cell adhesion in blood flow and the adhesion of capsules or cells in microfluidic devices.

1.3 Literature survey: droplet deformation

The pioneering work of Taylor[34, 35] was the first experimental and theoretical analysis on the deformation and orientation of droplets in shearing flows. Since then, numerous theoretical and experimental studies have been conducted on this topic. Summaries can be found in the two review papers by Rallison[26] and Stone[31].

This problem depends on two dimensionless parameters: (a) the ratio of the viscosity of the fluid inside the drop to that of the external fluid λ, and (b) the capillary number $Ca = \mu G\alpha/\gamma$, where μ is the viscosity of the external fluid, G is the shear rate of the flow outside, α is a characteristic length of the droplet, and γ is the interfacial surface tension.

Taylor[35] compared his first-order theoretical results with his experimental findings; good agreement was found for small deformations. A slender-body theory was derived by Taylor[36] to investigate large deformations.

Numerous numerical methodologies have been employed for the study of deforming droplets. Youngren and Acrivos[37] were the first to develop a Boundary Integral method and determine the equilibrium shape of a droplet for $\lambda = 0$ in an axisymmetric extensional flow. Rallison and Acrivos[24], and Rallison[25] calculated the case of $\lambda > 0$ for an extensional flow and $\lambda = 1$ for non-axisymmetric shear flows. Navot[21] studied the critical dynamics of the droplet breakup under axisym-

metric viscous flows for $\lambda = 1$. A two-dimensional droplet model was setup based on an equi-distant partition of the interfacial curve. Roumeliotis and Fulford[30] adopted cubic splines to represent the interfacial curve in the two-dimensional problem they studied. Besides numerical methods, complex variables were used by Richardson[28, 29] to study the case of $\lambda = 0$ for two-dimensional droplets. Buckmaster and Flaherty[2] also studied a deforming two-dimensional droplet for $\lambda = 1$.

In order to fully understand the droplet deformation, three-dimensional models have been set up recently. The Boundary Integral algorithm is usually applied which requires only the information on the interface and solves for the velocity or the force on the boundary. Thus, it reduces the dimensionality of the problem by one, which facilitates considerably the computations. Zinchenko, Rother and Davis[38] described a system of deformable droplets in a viscous medium at low-Reynolds numbers, especially the interaction of two droplets and their buoyancy driven motions. They employed a paraboloid fitting algorithm as the mesh stabilization method to solve a curvatureless Boundary Integral equation. They studied droplets with $\lambda = 1$ or $\lambda \to 0$ in a buoyancy-driven flow for $Ca = 0.723$. The interaction of droplets was also studied for $Ca = 0.35$ and $\lambda = 0.2$. Cristini, Blawzdziewicz and Loewenberg[4] developed an adaptive discretization algorithm to solve the three-dimensional Boundary Integral equations of the evolving droplet surface. The deformation was studied under shear flows. Equilibrium shapes were found for $Ca = 1.43$, $\lambda = 3$, and for $Ca = 0.8$, $\lambda = 0.01$. Feigl *et al.*[13] calculated the deformation of a liquid drop suspended in a flow field ranging from shear flow to uniaxial elongation flow. When $\lambda = 1$ or $\lambda = 5$, the critical capillary number was

found to be a function of the flow types. Cunhua and Loewenberg[5] modified the adaptive surface triangulation algorithm proposed by Cristini, Blawzdziewicz and Loewenberg[4]. They computed the interaction between a pair of droplets suspended in Stokes flow and compared their results with experimental findings for $\lambda = 1.4$ and $Ca = 0.13$. A nonsingular contour-integral representation of the layer potentials was employed by Bazhlekov, Anderson and Meijer[1] to calculate the droplet deformation. The authors employed a multiple-step time-integration scheme to calculate the deformation as a function of time for $\lambda = 1$ and $Ca = 0.05$ in a 2D extensional flow.

1.4 Literature survey: Stokes flow over a hump

Higdon[17] studied the problem of a viscous flow over a protuberance or depression on a solid surface by a two-dimensional Boundary Element method. The stress distribution and the streamline behavior were determined for various geometrical configurations. Gaver and Kute[14] set up a two-dimensional geometry of a semi-circle bulge on a channel within two parallel plates. A pressure-driven flow was assumed and the lubrication theory was employed to validate the numerical results. A wide ranges of cell sizes with respect to the channel size were studied. The stress, force and torque exerted on the cell were analyzed. Regression relationships between the size, flow rate and the force were established.

The adhesion of a biological cell onto a substrate, the interaction among adhered cells and the influence of the fluid force on endothelial cells have been deter-

mined mainly via three-dimensional computations. Pozrikidis[23] restated the problem by Gaver and Kute[14] in three dimensions for the case of 2D Hagen-Poiseuille flow or a pure shear flow. Streamlines and shear stress distributions on the protuberance and the depression were determined. The torque and force coefficients were found for various contact angles. Hazel and Pedley[16] numerically solved for a three-dimensional protuberance in a large circular tube. The tube was simplified into an infinite solid plane and a quasi-steady linear shear flow was assumed. This is actually a three-dimensional model for the problem studied by Higdon[17]. The hump was assumed to be ellipsoidal. Several combinations of the height, length and the width of the hump were applied to determine the geometry which minimizes the total force on the hump. Sugihara-Seki[32] compared the shear stress and pressure distribution exerted on a spherical cell adhered to the microvessel wall in tube flow and those in parallel-plate flow. Sugihara-Seki and Schmid-Schonbein[33] estimated and compared the fluid shear stress on the attached cell (leukocyte) and the shear stress on a free-suspended cell in a micro-vessels. Brooks and Tozeren[3] employed a finite-difference scheme to analyze the laminar parallel-plate flow past an array of uniformly distributed cells that were adherent to the bottom plate. The fluid forces on the cell were computed under different cell conditions, i.e., different combinations of the aspect ratio of the cell radius to the gap between the parallel plates and contact angles of the spreading cell.

1.5 Summary of current research

The current thesis includes two distinct projects. The first study involves the development of a novel three-dimensional Spectral Boundary Element algorithm for interfacial dynamics in Stokes flow. The main attraction of this approach is that it exploits all the benefits of the spectral methods (i.e., exponential convergence and numerical stability) with the versatility of the finite element method (i.e., the ability to handle the most complicated geometries). In addition, it is not affected by the disadvantage of the spectral methods used in volume discretization; namely, the requirement of deal with dense systems, because in boundary integral formulations the resulting systems are always dense, independent of the form of the discretization. Our method also exploits all the benefits of the boundary element techniques, i.e., reduction of the problem dimensionality and great parallel scalability. Our algorithm is the only available high-order/high-accuracy methodology for the problem of droplet deformation in viscous flows. By applying this algorithm to several interfacial problems in extensional and shear flows, we find that our results are in excellent agreement with experimental findings, analytical predictions and previous numerical computations. This algorithm can be employed to study a wide range of interfacial problems in Stokes flow including the deformation of capsules and blood cells in micro-vessels.

Our Spectral Boundary Element method is also employed to analyze the shear stress, drag and torque exerted on a protuberance on the inner wall of a micro-tube. In contrast to previous studies, a cylindrical tube is defined, and a three-dimensional

Hagen-Poiseuille flow is considered. This feature enables the current model to apply to both microfluidics and microcirculation where the curvature of the tube/vessel can not be ignored due to the comparable size of the tube/vessel and the hump. In physiological systems, the protuberance may represent leukocytes (white blood cells), blood clots or endothelial cells attached to the inner surface of microvessels. Therefore, our study facilitates the understanding of mechano-transduction phenomena (which involve the relation between the hemodynamic shear force received by endothelial cells and the chemical signals they send out) as well as the leukocyte/endothelial cell adhesion in blood flow. The algorithm developed here will be adopted for the study of the deformation of capsules and blood cells in constricted geometries.

The first project, the development of a three-dimensional interfacial dynamics Spectral Boundary Element algorithm, along with the relevant work by Jingtao Wang in two dimensions, has been presented in both national and international conferences (such as the 2004 AIChE Annual Meeting and the 5th Euromech Fluid Mechanics Conference), and it will be submitted for publication in the near future. The second project which studies the stress on a protuberance in microtubes has been presented in the 2004 AIChE Annual Meeting and the 2004 Inaugural Symposium of the Burgers Program for Fluid Dynamics. It will also be presented in the 76th Annual Meeting of the Society of Rheology and be submitted for publication.

Chapter 2

Mathematical Formulation

2.1 From Stokes equations to Boundary Integral equations

When the Reynolds number is sufficiently small, the inertial terms in the Navier-Stokes equations are neglected and the flow is governed by Stokes equations

$$\nabla \cdot \boldsymbol{\sigma} \equiv -\nabla p + \mu \nabla^2 \boldsymbol{u} = 0 \tag{2.1}$$

and the continuity equation

$$\nabla \cdot \boldsymbol{u} = 0 \tag{2.2}$$

where $\boldsymbol{\sigma}$ represents the stress tensor, p is the dynamic pressure, μ is the viscosity of the fluid and $\boldsymbol{u}$ is the velocity vector.

By introducing the fundamental solutions S_{ij} and T_{ijk} for the three-dimensional Stokes equation (2.1) and the continuity equation (2.2), and then integrating over a volume of fluid bounded by a surface S_B shown in figure 2.1(a), the velocity at a point $\boldsymbol{x}_0$ on the surface is expressed as the following Boundary Integral equation (BIE),

$$u_i(\boldsymbol{x_0}) = -\frac{1}{4\pi\mu} \int_{S_B} \left(S_{ij}(\hat{\boldsymbol{x}}) f_j(\boldsymbol{x}) - \mu T_{ijk}(\hat{\boldsymbol{x}}) u_j(\boldsymbol{x}) n_k(\boldsymbol{x}) \right) dS \tag{2.3}$$

This equation relates the velocity $\boldsymbol{u}$ at each point $\boldsymbol{x_0}$ along the boundary S_B by the

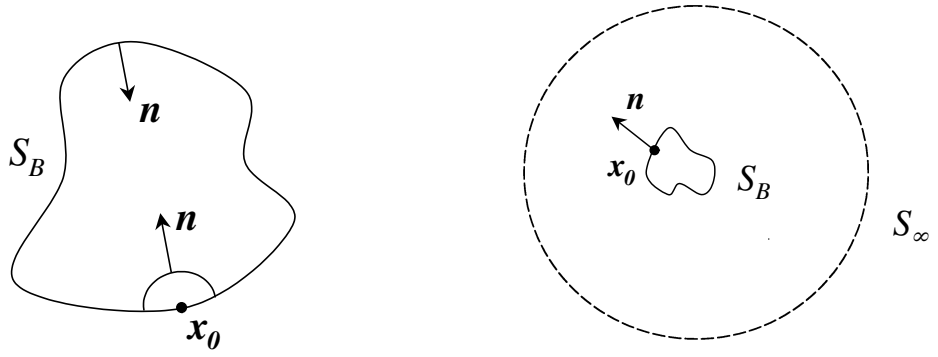

(a) (b)

Figure 2.1: Illustrations for the geometry of the BIEs (2.3) and (2.6).

surface integral of the stress and velocity over all the points $\boldsymbol{x}$ on the same boundary. The normal vector $\boldsymbol{n}$ points into the domain surrounded by the boundary S_B while the force vector $\boldsymbol{f}$ is defined by $f_j(\boldsymbol{x}) = \sigma_{jk}(\boldsymbol{x})n_k(\boldsymbol{x})$. The fundamental solution for the velocity S_{ij} and the corresponding stress T_{ijk} are given by

$$S_{ij} = \frac{\delta_{ij}}{r} + \frac{\hat{x}_i\hat{x}_j}{r^3} \tag{2.4}$$

$$T_{ijk} = -6\frac{\hat{x}_i\hat{x}_j\hat{x}_k}{r^5} \tag{2.5}$$

A detailed derivation may be found in Pozrikidis[22].

Equation (2.3) can be named as the "inner" equation because it solves for the fluid flow inside a specific boundary S_B shown in figure 2.1(a). An "outer" equation can be derived to express the flow field outside a boundary S_B shown in figure 2.1(b). It is given by

$$\boldsymbol{u}(\boldsymbol{x}_0) - 2\boldsymbol{u}^\infty(\boldsymbol{x}_0) = -\frac{1}{4\pi\mu}\int_{S_B}(\boldsymbol{S}\cdot\boldsymbol{f} - \mu\boldsymbol{T}\cdot\boldsymbol{u}\cdot\boldsymbol{n})\,dS \tag{2.6}$$

where $\boldsymbol{u}^{\infty}$ is the fluid velocity far from the surface boundary S_B and the normal vector $\boldsymbol{n}$ points into the flow (i.e., out of the boundary S_B).

2.2 BIE for a free suspended drop

Consider the case of a droplet with density ρ_1 and viscosity $\mu_1 = \lambda\mu$ suspended in an infinite fluid with density ρ_2 and viscosity $\mu_2 = \mu$, as illustrated in figure 2.2. The interfacial tension γ is assumed to be constant while $\boldsymbol{u}^{\infty}$ is the flow velocity far from the droplet interface S_B. The magnitude of the gravity acceleration is g. The normal vector $\boldsymbol{n}$ points into the fluid outside the interface S_B.

The interior fluid is driven to flow by the exterior flow. The "inner" and "outer" equations (2.3) and (2.6) now apply to the interior and exterior domains, respectively. The "inner" equation has to change sign due to the direction of the normal vector. After subtracting equation (2.3) from equation (2.6), the velocity of the point $\boldsymbol{x}_0$ on the interface S_B is expressed as

$$\begin{aligned} &(1+\lambda)\boldsymbol{u}(\boldsymbol{x}_0) - 2\boldsymbol{u}^{\infty}(\boldsymbol{x}_0) \\ &= -\frac{1}{4\pi\mu}\int_{S_B} (\boldsymbol{S}\cdot\Delta\boldsymbol{f} - \mu(1-\lambda)\boldsymbol{T}\cdot\boldsymbol{u}\cdot\boldsymbol{n})\, dS \end{aligned} \tag{2.7}$$

where the velocity $\boldsymbol{u}$ and the jump of the interfacial stress $\Delta\boldsymbol{f}$ come from the interfacial boundary conditions:

$$\boldsymbol{u} = \boldsymbol{u}_1 = \boldsymbol{u}_2 \tag{2.8}$$

$$\Delta\boldsymbol{f} \equiv \boldsymbol{f}_2 - \boldsymbol{f}_1 = \gamma(\nabla\cdot\boldsymbol{n})\boldsymbol{n} + (\rho_2 - \rho_1)(\boldsymbol{g}\cdot\boldsymbol{x})\boldsymbol{n} \tag{2.9}$$

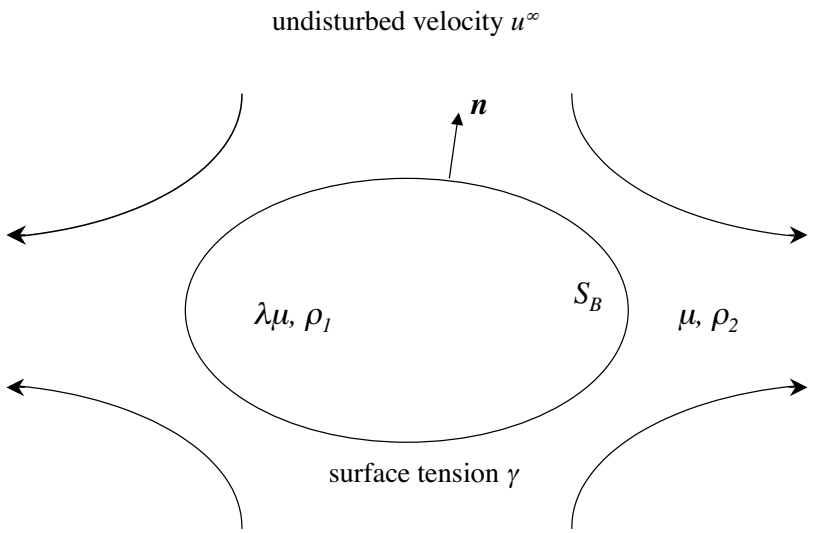

Figure 2.2: Illustration of a droplet freely suspended in an infinite fluid.

where the subscripts "1" and "2" represent the internal and external flow, respectively. If $\Delta \boldsymbol{f}$ is known, equation (2.7) becomes a Fredholm integral equation of the second kind in solving for the interfacial velocity $\boldsymbol{u}$.

2.3 BIE for a drop in a confined domain

We can imagine two cases involving a drop in a confined domain. One is the situation where a drop is suspended in an external fluid enclosed by an outer solid boundary (figure 2.3). The other case involves a drop attached to a solid wall (figure 2.4). Because the first case can be considered as a simplification of the second one, we first discuss the construction of the Boundary Integral equations for the second case.

As shown in figure 2.4, a drop with viscosity $\lambda\mu$ and density ρ_1 is attached to the internal surface of a cylindrical tube. The fluid external to the drop has viscosity μ and density ρ_2 while far from the droplet it shows undisturbed velocity $\boldsymbol{u}^\infty$ and

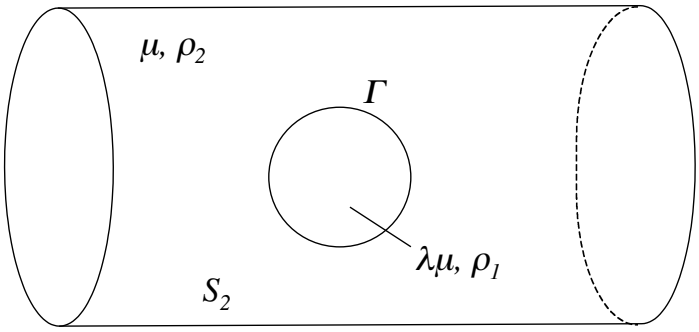

Figure 2.3: Illustration of a drop suspended in the fluid inside a cylindrical tube (S_2).

stress $\boldsymbol{f}^{\infty}$. We denote the interface between the drop and the external fluid as Γ, the wetted area of the drop and the solid as S_1, and the rest boundary surface as S_2, which is composed by S_2^f and S_2^w. S_2^f is a fluid boundary and it is assumed to be far away from the drop. S_2^w refers to the rest solid boundary. The surface tension on the interface Γ is γ and the magnitude of the gravity acceleration is g. We also denote $\boldsymbol{u}_1$ and $\boldsymbol{u}_2$ as the flow velocity inside and outside of the drop, respectively. The boundary conditions on surface S are

$$\boldsymbol{u}_1 = 0 \quad \text{on boundary } S_1 \tag{2.10}$$

$$\boldsymbol{u}_2 = 0 \quad \text{on boundary } S_2^w \tag{2.11}$$

$$\boldsymbol{u}_2 = \boldsymbol{u}^{\infty} \quad \text{or} \quad \boldsymbol{f}_2 = \boldsymbol{f}^{\infty} \quad \text{on boundary } S_2^f \tag{2.12}$$

The boundary conditions on Γ are given by equations (2.8) and (2.9).

By applying the governing equation (2.3) on the fluid flow both inside and outside the drop, and then performing a subtraction between the two equations, a

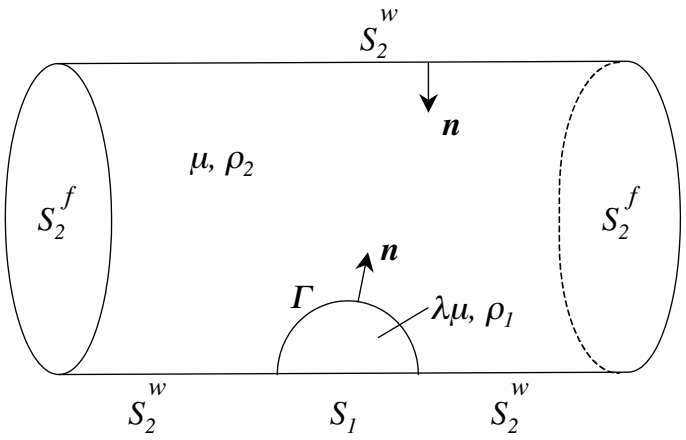

Figure 2.4: Illustration of a drop adherent to a solid cylindrical boundary.

general Boundary Integral equation for both flow regions can be derived as

$$\begin{aligned}\Omega \boldsymbol{u}(\boldsymbol{x}_0) &= -\int_{S_2} [\boldsymbol{S}\cdot\boldsymbol{f}_2 - \mu \boldsymbol{T}\cdot\boldsymbol{u}_2\cdot\boldsymbol{n}]\, dS \\ &\quad + \int_{S_1} [\boldsymbol{S}\cdot\boldsymbol{f}_1 - \lambda\mu \boldsymbol{T}\cdot\boldsymbol{u}_1\cdot\boldsymbol{n}]\, dS \\ &\quad - \int_{\Gamma} [\boldsymbol{S}\cdot\Delta\boldsymbol{f} - (1-\lambda)\mu \boldsymbol{T}\cdot\boldsymbol{u}\cdot\boldsymbol{n}]\, dS \end{aligned} \tag{2.13}$$

where the subscripts "1" and "2" refer to fluids inside and outside of the drop, respectively. In the third term on the right-hand side, the velocity is $\boldsymbol{u} = \boldsymbol{u}_1 = \boldsymbol{u}_2$. For points on Γ, $\Omega = 4\pi(1+\lambda)\mu$; for points on S_1, $\Omega = 4\pi\lambda\mu$; for points on S_2, $\Omega = 4\pi\mu$. A system of Fredholm integral equations of mixed kinds is formed due to the different boundary conditions.

Another construction of the BIE can be set up by employing the disturbed velocity $\boldsymbol{u}^D$ and the disturbed force $\boldsymbol{f}^D$ in the "inner" equation (2.3) for the flow inside the tube but outside the drop, where $\boldsymbol{u}^D = \boldsymbol{u} - \boldsymbol{u}^\infty$ and $\boldsymbol{f}^D = \boldsymbol{f} - \boldsymbol{f}^\infty$. Based on our assumption, $\boldsymbol{u}^D$ and $\boldsymbol{f}^D$ are zero on the fluid boundary S_2^f, so that

the integration on S_2^f disappears. Equation (2.3) is then transformed into

$$\boldsymbol{u}^D(\boldsymbol{x_0}) = -\frac{1}{4\pi\mu}\int_{\Gamma+S_2^w}\left(\boldsymbol{S}\cdot\boldsymbol{f}^D - \mu\boldsymbol{T}\cdot\boldsymbol{u}^D\cdot\boldsymbol{n}\right)dS \tag{2.14}$$

By applying the governing equation (2.3) on the flow inside the drop, changing its sign (due to the direction of the normal vector on the boundary), and subtracting it from equation (2.14), the BIE describing the system takes the form

$$\begin{aligned}\Omega\boldsymbol{u}(\boldsymbol{x}_0) - \Omega_0\boldsymbol{u}^\infty(\boldsymbol{x}_0) &= -\int_\Gamma\left[\boldsymbol{S}\cdot(\Delta\boldsymbol{f} - \boldsymbol{f}^\infty) - \mu\boldsymbol{T}\cdot(\boldsymbol{u}(1-\lambda) - \boldsymbol{u}^\infty)\cdot\boldsymbol{n}\right]dS \\ &\quad -\int_{S_2^w}\left[\boldsymbol{S}\cdot(\boldsymbol{f}_2 - \boldsymbol{f}^\infty) - \mu\boldsymbol{T}\cdot(\boldsymbol{u}_2 - \boldsymbol{u}^\infty)\cdot\boldsymbol{n}\right]dS \\ &\quad +\int_{S_1}\left[\boldsymbol{S}\cdot\boldsymbol{f}_1 - \lambda\mu\boldsymbol{T}\cdot\boldsymbol{u}_1\cdot\boldsymbol{n}\right]dS \end{aligned}\tag{2.15}$$

where $\Omega = 4\pi\mu(1+\lambda)$, $4\pi\mu\lambda$ and $4\pi\mu$ for $\boldsymbol{x_0}$ on Γ, S_1 and S_2^w, respectively; $\Omega_0 = 4\pi\mu$, 0, and $4\pi\mu$ for $\boldsymbol{x_0}$ on Γ, S_1 and S_2^w respectively. The boundary conditions (2.8, 2.9, 2.10, and 2.11) are applied.

Although equations (2.13) and (2.15) are two different BIEs for a drop in a confined domain, they result in similar solutions. Note that when the boundary S_1 vanishes, i.e., the droplet is freely suspended (shown in figure 2.3), the integral over S_1 on the right-hand side of equation (2.13) and (2.15) disappears.

2.4 BIE for flow in a cylinder with a protuberance

If the protuberance in the cylindrical tube is assumed solid, the Boundary Integral equation for the flow can simply take the form of the "inner" equation (2.3). There are two kinds of boundaries: one is the solid wall, and the other is the fluid boundary

S_2^f (figure 2.4). Based on our assumption, the boundary conditions are

$$\boldsymbol{u} = 0 \quad \text{on boundaries } S_2^w \text{ and } \Gamma \tag{2.16}$$

$$\boldsymbol{u} = \boldsymbol{u}^\infty \quad \text{or} \quad \boldsymbol{f} = \boldsymbol{f}^\infty \quad \text{on boundary } S_2^f \tag{2.17}$$

The BIE can also be expressed with respect to the disturbed velocity $\boldsymbol{u}^D$ and the disturbed force $\boldsymbol{f}^D$. It takes the form of equation (2.14).

2.5 Spectral element formulation

The Boundary Integral equations are solved using the Spectral Boundary Element method as described in Muldowney and Higdon [20]. Its accuracy, efficiency and convergence have been demonstrated in applications involving rigid particles, deformable droplets and interacting particles. Higdon and Muldowney [18] applied this method in the study of the resistance functions for Stokes flow past spherical particles, droplets and bubbles in cylindrical tubes. Dimitrakopoulos and Higdon employed both the 2D [7] and 3D [8, 10, 11, 12] Boundary Element methods in studies on the displacement of droplet from solid surfaces in Stokes flows.

According to this method, the boundary is divided into a moderate number N_E of surface elements, each of which is mapped onto a two-dimensional domain in terms of the parametric variables ξ and η. The variables are zeros of orthogonal polynomials, such as Legendre, Chebyshev or Jacobi polynomials, on $[-1, 1]$. If N_B basis points are used, then the geometry $\boldsymbol{x}$ can be represented by

$$\boldsymbol{x}(\xi, \eta) = \sum_{i=1}^{N_B} \sum_{j=1}^{N_B} \boldsymbol{x}(\xi_i, \eta_j) h_j(\eta) h_i(\xi) \tag{2.18}$$

where $h_i(\xi)$ and $h_j(\eta)$ are the $(N_B - 1)$-order Lagrangian interpolant polynomial. The physical variables $\boldsymbol{u}$ and $\boldsymbol{f}$ are represented similarly.

The discretized expressions for the geometry and the physical variables are substituted into the Boundary Integral equations, and it is required that the integral equations be satisfied at the discrete set of basis points $\boldsymbol{x}_0(\xi_i, \eta_j)$ (where $i, j = 1, \ldots, N_B$) on each spectral element. This yields a linear system of $3N_E\, N_B^2$ algebraic equations

$$\boldsymbol{u} = \boldsymbol{A}\boldsymbol{f} + \boldsymbol{B}\boldsymbol{u} \tag{2.19}$$

The system matrices $\boldsymbol{A}$ and $\boldsymbol{B}$ are defined as integrals of the kernels $\boldsymbol{S}$ and $\boldsymbol{T}$ (see equations (2.4) and (2.5)) and the basis functions over the set of the surface elements. The numerical integration is performed by Gauss-Legendre quadrature with the aid of variable transformations. Owing to the singularity in the kernels, special care must be taken to ensure the accurate numerical evaluation of these integrations as described in Muldowney and Higdon[20].

The BIEs, combined with the boundary data at the $N_E\, N_B^2$ basis points, yield, for a known interface, a consistent set of $3N_E\, N_B^2$ equations in $3N_E\, N_B^2$ unknowns which is solved using Gaussian elimination since the system matrix is dense.

Chapter 3

Interfacial Dynamics in Stokes Flow

If the shear rate of the flow is below a certain critical value, the surface tension force and the external viscous force on the drop interface can balance each other, and an equilibrium state can be reached. Otherwise the drop bursts and produces two or more daughter droplets. How much distortion is reached at equilibrium and how the droplet deforms with time are among the principal goals of both experimental and theoretical studies in this area.

In this chapter, we develop a novel three-dimensional Spectral Boundary Element method for interfacial dynamics in Stokes flow. This algorithm is the only available high-order/high-accuracy methodology for the problem of droplet deformation in viscous flows. By applying this algorithm to several interfacial problems, we find that our results are in excellent agreement with experimental findings, analytical predictions and previous numerical computations.

3.1 Problem parameters and dimensionless analysis

The problem of interfacial dynamics in Stokes flow is governed by two dimensionless numbers: the viscosity ratio λ and the capillary number Ca given by

$$\lambda = \frac{\mu_1}{\mu} \tag{3.1}$$

$$Ca = \frac{\mu G \alpha}{\gamma} \tag{3.2}$$

where μ_1 is the viscosity of the fluid inside the drop, μ is the viscosity of the imposed flow, and γ is the surface tension on the interface. The constant G designates the shear rate of the external flow and α is the characteristic length of the droplet defined from the drop volume V as

$$\alpha = \left(\frac{3V}{4\pi}\right)^{1/3} \tag{3.3}$$

The capillary number Ca measures two competing forces: the viscous force and the surface tension force. The viscous stress imposed on the interface by the exterior flow induces the flow inside the drop and causes the interfacial deformation, while the surface tension force resists the deformation. When an equilibrium state is reached, the surface tension force balances the viscous force so that the droplet deformation ceases. Figure 3.1 illustrates that a droplet of viscosity $\mu_1 = \lambda\mu$ and density ρ_1 deforms in an extensional flow of a fluid with viscosity μ and density ρ_2. (In this study we assume that $\rho_1 = \rho_2$.) The undisturbed velocity of the exterior fluid is designated as $\boldsymbol{u}^\infty$. The droplet deforms from an initially spherical shape at time t_0 to an ellipsoid-like shape at time t_1. The degree of deformation is measured via the

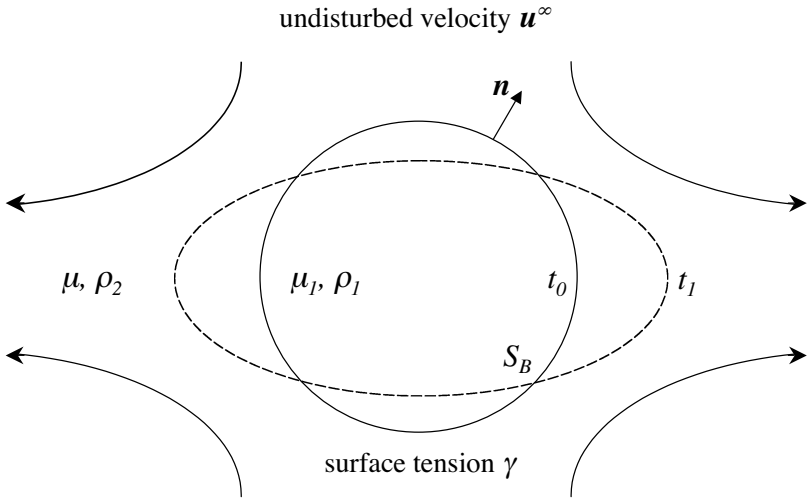

Figure 3.1: Illustration for the deformation of a droplet in an extensional flow.

parameter D defined by

$$D = \frac{L - S}{L + S} \tag{3.4}$$

where L is the length of the longest axis of the drop and S is that of the shortest axis. We identify the characteristic length of the drop α as the length scale of the problem, the velocity scale is $G\alpha$, and the time scale is $1/G$. In this chapter we use dimensionless variables thereafter.

3.2 Time-integration algorithm

We consider a three-dimensional droplet suspended in an infinite fluid undergoing a low-Reynolds-number shearing flow. The governing equations are the Stokes equations along with the continuity equation. Earlier in Chapter 2, we described the corresponding Boundary Integral equation (2.7) and the boundary conditions (2.8) and (2.9) for a freely suspended droplet. The drop interface is discretized into

$N_E = 6$ elements with $N_B \times N_B = 12 \times 12$ spectral basis points on each element. These points are of Lobatto type, i.e., end points along with interior points, while there is no connection between elements. The spectral element formulation has been discussed in section 2.5. For a given droplet geometry, the velocity on the droplet interface is obtained by the Spectral Boundary Element method described in Chapter 2.

In order to determine the shape of the drop as a function of time, a time-integration algorithm is employed to solve the kinematic condition at the interface

$$\frac{\mathrm{d}\boldsymbol{x}}{\mathrm{d}t} = (\boldsymbol{u} \cdot \boldsymbol{n})\boldsymbol{n} \tag{3.5}$$

For this, we determine the interfacial velocity $\boldsymbol{u}$ of the known shape $\boldsymbol{x}(t)$ from BIE (2.7), and then the discretized points of the droplet interface are advanced by a time interval Δt to obtain the shape $\boldsymbol{x}(t+\Delta t)$. An explicit Euler or Runge-Kutta method is employed for the time-integration. The explicit Euler scheme can be written as

$$\boldsymbol{x}(t + \Delta t) = \boldsymbol{x}(t) + \Delta t(\boldsymbol{u} \cdot \boldsymbol{n})\boldsymbol{n} \tag{3.6}$$

where $\boldsymbol{n}$ is the normal vector of the known shape $\boldsymbol{x}(t)$. We note that explicit time-integration schemes have commonly been employed with various discretization methods, e.g. Feigl, Kaufmann, Fischer and Windhab[13], Rallison and Acrivos[24], Rallison[25], and Roumeliotis and Fulford[30].

If we apply the advancing scheme described above without any geometric constraints, the resulting algorithm is unstable even after only a small number of steps. Geometrically, the instability is caused by the discontinuity at the edges of the spectral elements and results in the breakup of the entire shape. Figure 3.2 shows the

deformation of a suspended droplet in a 2D extensional flow at four different times, for capillary number $Ca = 0.2$ and viscosity ratio $\lambda = 0.01$. The number of time steps is denoted as N_{st} while u_n is the maximum normal velocity at the interface. The discontinuity on the element edges can be witnessed in figure 3.2(d) and the droplet interface breaks at the step $N_{st} = 156$, i.e., the time $t = 0.312$.

A first-order smoothing technique is derived to resolve this problem. In every time step, the smoothing scheme adjusts the grid of each element so that the position, the tangent and the normal vectors on the element edges are continuous across the spectral elements. The next section describes our novel smoothing method in detail.

3.3 First-order smoothing scheme

Our first-order smoothing scheme eliminates the discrepancies in the position, the tangent and normal vectors at the element edges across the spectral elements which are caused by the numerical advancing of the interface. In this section, we first describe how we smooth the position, the tangent and normal vectors at the element edges and then we explain how we update the position for all the points on each spectral element by a two-dimensional Hermitian interpolation.

Let the non-smoothed interfacial shape at time $t + \Delta t$, derived by the time integration of equation (3.5) above, be identified as $\boldsymbol{x}(\xi,\eta)$ where ξ and η are the two parametric variables describing the interface. We also define a local Cartesian coordinate system $\boldsymbol{x}^L$ at each point with the x_1^L- and x_2^L-axes in the tangent plane

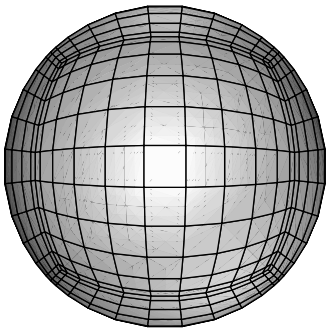

(a) $N_{st} = 0$, time $t = 0.000$,

D= 0.000D+00, u_n= 0.159D+01

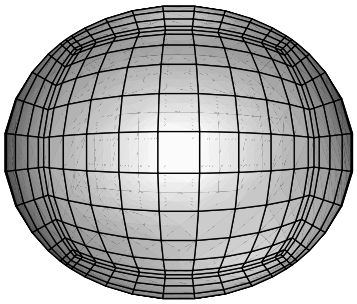

(b) $N_{st} = 30$, time $t = 0.060$,

D= 0.877D-01, u_n= 0.133D+01

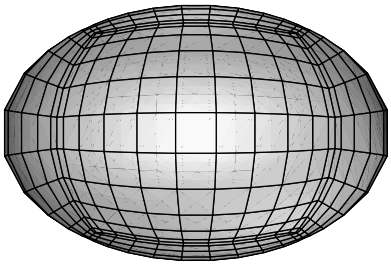

(c) $N_{st} = 90$, time $t = 0.180$,

D=0.206D+00, u_n=0.890D+00

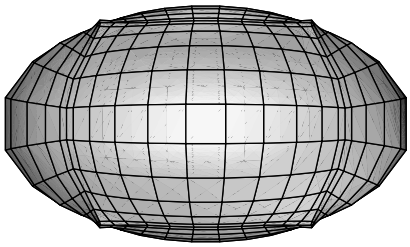

(d) $N_{st} = 140$, time $t = 0.280$,

D= 0.268D+00, u_n= -0.281D+03

Figure 3.2: The time evolution of a drop deforming in a 2D extensional flow for $Ca = 0.2$ and $\lambda = 0.01$. A 4th-order Runge-Kutta (RK4) method without interfacial smoothing is employed with $N_E = 6$, $N_B = 12$ and $\Delta t = 2 \times 10^{-3}$.

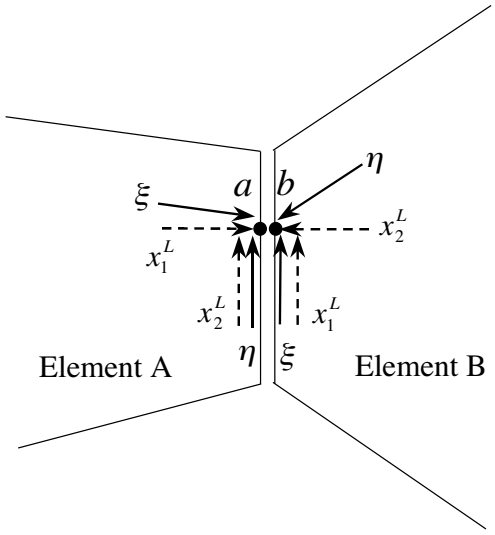

Figure 3.3: Illustration for the curvilinear coordinates (ξ, η) and the local Cartesian coordinates (x_1^L, x_2^L). Two neighbor elements A and B are displayed. The points a and b are two coincident points belonging to elements A and B, respectively, and should overlap after the interfacial smoothing.

and the x_3^L-axis parallel to the normal vector $\boldsymbol{n}$. As shown in figure 3.3, the points a and b are two coincident points belonging to the consecutive elements A and B, respectively. The solid arrows represent the curvilinear coordinates (ξ, η) and the dashed arrows the local Cartesian coordinates (x_1^L, x_2^L). The normal vector $\boldsymbol{n}$ and the third local Cartesian coordinate x_3^L are not plotted. In the situation illustrated, the parametric variable η at the point a coincides with the variable ξ at the point b and they both point at the same direction. In fact, due to the surface discretization, other combinations are possible, e.g. ξ at the point a coincides with ξ at the point b in the opposite direction.

To perform the interfacial smoothing, we first average the position $\boldsymbol{x}$ of the

edge points across neighbor elements

$$\boldsymbol{x}_a^{new} = \boldsymbol{x}_b^{new} = 0.5\,(\boldsymbol{x}_a^{old} + \boldsymbol{x}_b^{old}) \tag{3.7}$$

and then we calculate the geometric properties of the updated shape $\boldsymbol{x}^{new}$. In this way, for our specific example the derivatives $(\partial\boldsymbol{x}/\partial\eta)_a$ and $(\partial\boldsymbol{x}/\partial\xi)_b$ are identical. We next calculate the unit tangent vector

$$(\boldsymbol{t}_1^L)_a = \frac{\left(\frac{\partial\boldsymbol{x}}{\partial\eta}\right)_a \times \boldsymbol{v}_a}{\left|\left(\frac{\partial\boldsymbol{x}}{\partial\eta}\right)_a \times \boldsymbol{v}_a\right|} \tag{3.8}$$

where $\boldsymbol{v}_a$ is the non-unit normal at point a, $\boldsymbol{v}_a = (\partial\boldsymbol{x}/\partial\xi)_a \times (\partial\boldsymbol{x}/\partial\eta)_a$. The unit tangent $(\boldsymbol{t}_2^L)_b$ is found in a similar way. Note that the tangent vectors $(\boldsymbol{t}_1^L)_a$ and $(\boldsymbol{t}_2^L)_b$ lie on the x_1^L-axis at the point a and the x_2^L-axis at the point b, respectively. In order to achieve continuity in this tangent direction, we average the unit tangent vectors,

$$(\boldsymbol{t}_1^L)_a^{new} = -(\boldsymbol{t}_2^L)_b^{new} = 0.5\left[(\boldsymbol{t}_1^L)_a^{old} - (\boldsymbol{t}_2^L)_b^{old}\right] \tag{3.9}$$

where the minus sign appears due to the specific geometry shown in figure 3.3.

At this point, both the position and the tangent vectors at the edge points are continuous. The next goal is to determine the updated first-order derivatives $(\partial\boldsymbol{x}/\partial\xi)_a^{new}$ and $(\partial\boldsymbol{x}/\partial\eta)_b^{new}$. From the tangent vectors, we calculate the unit normal vectors

$$\boldsymbol{n}_a^{new} = \frac{(\boldsymbol{t}_1^L)_a^{new} \times \left(\frac{\partial\boldsymbol{x}}{\partial\eta}\right)_a}{\left|(\boldsymbol{t}_1^L)_a^{new} \times \left(\frac{\partial\boldsymbol{x}}{\partial\eta}\right)_a\right|} \tag{3.10}$$

$$\boldsymbol{n}_b^{new} = \frac{\left(\frac{\partial\boldsymbol{x}}{\partial\xi}\right)_b \times (\boldsymbol{t}_2^L)_b^{new}}{\left|\left(\frac{\partial\boldsymbol{x}}{\partial\xi}\right)_b \times (\boldsymbol{t}_2^L)_b^{new}\right|} \tag{3.11}$$

Note that $\boldsymbol{n}_a^{new}$ and $\boldsymbol{n}_b^{new}$ are identical now due to the interfacial smoothing we have performed. In order to calculate the updated derivative $(\partial\boldsymbol{x}/\partial\xi)_a^{new}$, the following

relations for the point a are applied

$$\boldsymbol{n}_a^{new} \cdot \left(\frac{\partial \boldsymbol{x}}{\partial \xi}\right)_a^{new} = 0 \tag{3.12}$$

$$\left(\frac{\partial \boldsymbol{x}}{\partial \xi}\right)_a^{new} \cdot \left(\frac{\partial \boldsymbol{x}}{\partial \eta}\right)_a = \left(\frac{\partial \boldsymbol{x}}{\partial \xi}\right)_a^{old} \cdot \left(\frac{\partial \boldsymbol{x}}{\partial \eta}\right)_a \tag{3.13}$$

$$\left|\left(\frac{\partial \boldsymbol{x}}{\partial \xi}\right)_a^{new}\right| = \left|\left(\frac{\partial \boldsymbol{x}}{\partial \xi}\right)_a^{old}\right| \tag{3.14}$$

The new derivative $(\partial \boldsymbol{x}/\partial \eta)_b^{new}$ can be found in a similar way.

So far, we have smoothed the position $\boldsymbol{x}$ and the first derivatives, $(\partial \boldsymbol{x}/\partial \xi)$ and $(\partial \boldsymbol{x}/\partial \eta)$, at the edge points across the spectral elements. We want to employ this updated information of the edge points to derive a smoothed interfacial shape. For this, we generate $(N_B - 4) \times (N_B - 4)$ interior Jacobi points from the $N_B \times N_B$ Lobatto points (i.e., end and interior points) on each spectral element. By combining these Jacobi points with the smoothed position $\boldsymbol{x}$ and the first-order derivatives $(\partial \boldsymbol{x}/\partial \xi)$ and $(\partial \boldsymbol{x}/\partial \eta)$ at the edge points, a two-dimensional Hermitian interpolation is employed to produce a new set of $N_B \times N_B$ Lobatto points which represents the final smoothed interfacial shape at time $t + \Delta t$. The two-dimensional Hermitian interpolation involves two nested one-dimensional Hermitian interpolations. The specific one-dimensional Hermitian interpolation was derived in Dimitrakopoulos[6]

and it is given by

$$
\begin{aligned}
f(x) = (x^2-1)^2 \sum_{i=1}^{M} \frac{1}{(x_i^2-1)^2} \prod_{j\neq i}^{M} \left(\frac{x-x_j}{x_i-x_j}\right) f(x_i) + \\
\prod_{j=1}^{M} \left(\frac{x-x_j}{-1-x_j}\right) \frac{(x-1)^2}{4}(x+1) f'(-1) + \\
\prod_{j=1}^{M} \left(\frac{x-x_j}{1-x_j}\right) \frac{(x+1)^2}{4}(x-1) f'(+1) + \\
\prod_{j=1}^{M} \left(\frac{x-x_j}{-1-x_j}\right) \frac{(x-1)^2}{4}[1+b_{(-1)}(x+1)] f(-1) + \\
\prod_{j=1}^{M} \left(\frac{x-x_j}{1-x_j}\right) \frac{(x+1)^2}{4}[1-b_{(+1)}(x-1)] f(+1)
\end{aligned} \tag{3.15}
$$

The function values $f(-1)$ and $f(+1)$ correspond to the refreshed position $\boldsymbol{x}$ of the edge points while the derivatives $f'(-1)$ and $f'(+1)$ correspond to the updated $(\partial \boldsymbol{x}/\partial \xi)$ or $(\partial \boldsymbol{x}/\partial \eta)$ of the edge points. The coefficients $b_{(-1)}$ and $b_{(+1)}$ are chosen to yield zero slope at the element edges,

$$
b_{(-1)} = -\left[\sum_{j=1}^{M} \left(\frac{1}{x-x_j}\right) + \frac{2}{x-1}\right]_{x=-1} = \sum_{j=1}^{M} \left(\frac{1}{1+x_j}\right) + 1 \tag{3.16}
$$

$$
b_{(+1)} = +\left[\sum_{j=1}^{M} \left(\frac{1}{x-x_j}\right) + \frac{2}{x+1}\right]_{x=+1} = \sum_{j=1}^{M} \left(\frac{1}{1-x_j}\right) + 1 \tag{3.17}
$$

We emphasize that, for each one-dimensional Hermitian interpolation, the position and the first derivative at the two edges count for 4 degrees of freedom which, combined with the $(N_B - 4)$ degrees of freedom of the interior Jacobi points, produce the same total number of degrees of freedom as the Lobatto points N_B.

As a summary, the procedure of our first-order smoothing technique is:

- By employing the governing BIE (2.7) and a time integration scheme for equation (3.5), a temporary shape at time $t + \Delta t$ is generated at $N_B \times N_B$ Lobatto points. The corresponding tangent and normal vectors are calculated.

- By averaging the positions and the local tangent vectors of the edge points with those of their coincident points on the neighbor elements, smoothed normal vectors $\boldsymbol{n}$ and first-order derivatives, $(\partial \boldsymbol{x}/\partial \xi)$ and $(\partial \boldsymbol{x}/\partial \eta)$, are achieved.

- A set of $(N_B - 4) \times (N_B - 4)$ interior Jacobi points are interpolated from the Lobatto points. By employing the 2D Hermitian interpolation with the smoothed position $\boldsymbol{x}$ and the derivatives $(\partial \boldsymbol{x}/\partial \xi)$ and $(\partial \boldsymbol{x}/\partial \eta)$ at the element edges along with the interior Jacobi points, a new set of $N_B \times N_B$ Lobatto points is determined.

- This new geometry has continuous position, tangent and normal vectors across the interfacial elements and constitutes the interfacial shape at time $t + \Delta t$.

We emphasize that by employing our first-order smoothing scheme, we formally achieve the continuity of the position and the tangent/normal vectors at the edges of the spectral elements. However, for the problems we have studied in this thesis, our results show that this technique also achieves the continuity of the curvature at the element edges, i.e., the second-order derivative of the interfacial geometry.

Figure 3.4 shows that, by applying the smoothing scheme, the continuity of the droplet interface is preserved. The capillary number and the viscosity ratio are the same with those in figure 3.2, i.e., $Ca = 0.2$ and $\lambda = 0.01$. In contrast to figure 3.2, at time $t = 0.280$, the elements on the droplet interface smoothly connect with each other and the drop doesn't breakup even until time $t = 7.07$ where we stop our computations.

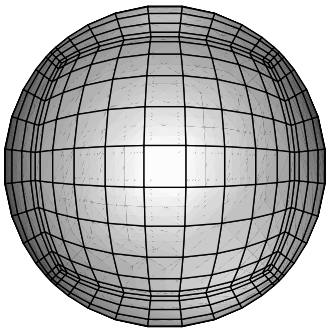

(a) $N_{st} = 0$, time $t = 0.000$,

D= 0.000D+00, u_n= 0.159D+01

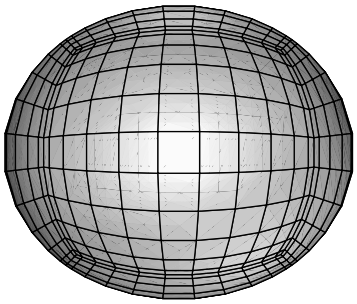

(b) $N_{st} = 30$, time $t = 0.060$,

D= 0.877D-01, u_n= 0.133D+01

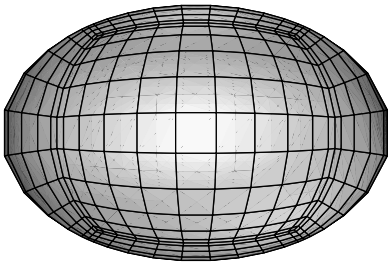

(c) $N_{st} = 90$, time $t = 0.180$,

D= 0.206D+00, u_n= 0.901D+00

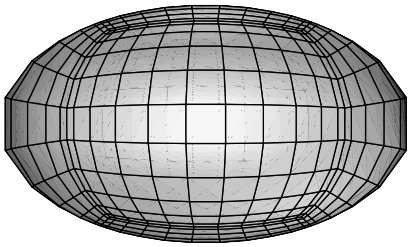

(d) $N_{st} = 140$, time $t = 0.280$,

D =0.267D+00, u_n= 0.663D+00

Figure 3.4: The time evolution of a drop deforming in a 2D extensional flow for $Ca = 0.2$ and $\lambda = 0.01$. An RK4 method with the 1st-order smoothing scheme is employed with $N_E = 6$, $N_B = 12$ and $\Delta t = 2 \times 10^{-3}$.

3.4 Results and discussion

By combining the Spectral Boundary Element method described in Chapter 2, an explicit time-integration scheme for equation (3.5) above, and the first-order smoothing technique described in section 3.2, we are able to calculate the transient droplet deformation for a wide array of interfacial problems. In this section, we consider the shape of the droplet during its course of deformation in a 2D extensional flow and a simple shear flow. In both cases, we investigate both small and large deformations as well as deformations for super-critical capillary numbers. We then examine the equilibrium state of the drop deformation for both flows. Comparisons are made with other numerical, theoretical or experimental results. All the results presented in this section are based on a 4th-order Runge-Kutta (RK4) time-integration algorithm combined with our 1st-order smoothing scheme.

3.4.1 Imposed planar extensional flow

For the droplet deformation in a 2D extensional flow with a shear rate G, the velocity far from the droplet is

$$\boldsymbol{u}^{\infty} = G \begin{pmatrix} 1 & 0 & 0 \\ 0 & -1 & 0 \\ 0 & 0 & 0 \end{pmatrix} \boldsymbol{x} = G\,(x, -y, 0) \tag{3.18}$$

while the lengths L and S of the droplet in equation (3.4) coincide with the major and minor axes on the intersection of the droplet and the XY plane, as shown in figure 3.5.

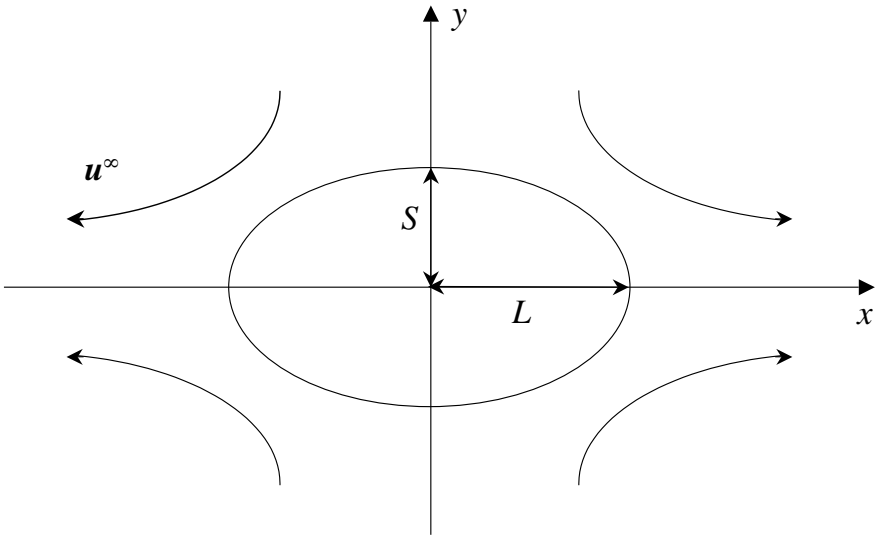

Figure 3.5: Illustration of a deforming drop in a 2D extensional flow.

In our computations, the drop starts to deform from the undisturbed spherical shape. One of the criteria to determine the equilibrium state in our computations is that the deformation D remains constant to at least six significant figures from one time step to the next one. Another criterion is that the magnitude of the normal velocity u_n in the final step should be small enough comparing to that of the undisturbed shape. In this study, the maximum normal velocity u_n of the final shape is at least $O(10^{-3})$ of the normal velocity of the undisturbed shape. This criterion even makes the deformation D remain constant at eight or more significant digits.

The time evolution of a drop in a 2D extensional flow with $Ca = 0.05$ and $\lambda = 20$ is shown in figure 3.6. The drop deforms fast at the beginning and then slows down until the deformation is stopped at the equilibrium. In contrast to the small deformation shown in figure 3.6, figure 3.7 shows a large deformation with $Ca = 0.1$ and $\lambda = 0.1$. The deformation achieves its equilibrium near time $t = 1$.

If the capillary number Ca exceeds the critical number for a specific viscosity ratio λ, the droplet follows an unsteady deformation until breakup. Figure 3.8 shows a large deformation with a super-critical capillary number $Ca = 0.2$ at a viscosity ratio $\lambda = 1.0$. In this case, there is no equilibrium state and the droplet breaks near time $t = 1.15$.

To validate our method, we compare the transient behavior of the deformation D from our computations with that from the nonsingular contour-integral method developed by Bazhlekov, Anderson and Meijer[1]. An excellent agreement is found, as shown in figure 3.9 where the deformation of a droplet in a 2D extensional flow is presented for $Ca = 0.05$ and $\lambda = 1.0$.

Dimitrakopoulos[9] derived a novel Newton iteration scheme for directly determining the interfacial equilibrium shape under flow conditions. The Newton method has shown its accuracy, efficiency and stability in numerous studies concerning the interfacial dynamics of droplets[7, 8, 9, 10, 11, 12]. In order to validate the accuracy of our transient method in predicting the equilibrium deformation D_E, a comparison of the transient method with the Newton method has been made in table 3.1. For a 2D extensional flow with $\lambda = 0.9$, the relative difference between the two methods is $O(10^{-5})$; for $\lambda = 20$, the relative difference is $O(10^{-3})$.

A first-order analytical estimation of the equilibrium deformation D_E of a droplet in an imposed 2D extensional flow was derived by Taylor[34],

$$D = 2\,Ca\,\frac{19\lambda + 16}{16\lambda + 16} \tag{3.19}$$

We emphasize that this relation is valid for small deformations only. The numerical

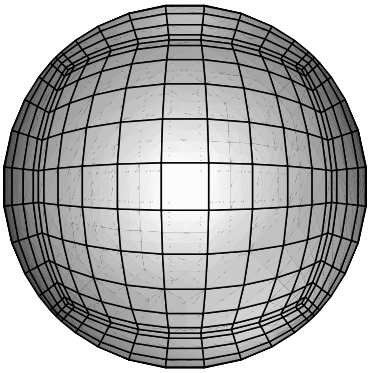

(a) N_{st}= 0, time t= 0.000,

D= 0.000D+00, u_n= 0.112D+00

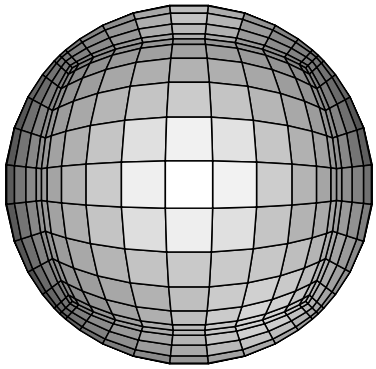

(b) N_{st}= 100, time t= 0.010,

D= 0.111D-01, u_n= 0.103D+00

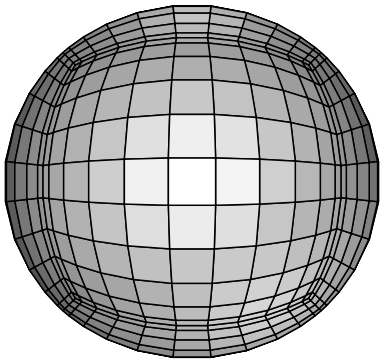

(c) N_{st}= 300, time t= 0.030,

D= 0.302D-01, u_n= 0.869D-01

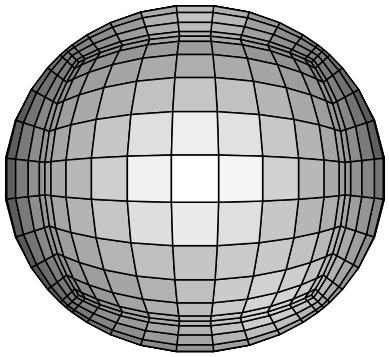

(d) N_{st}= 500, time t= 0.050,

D= 0.459D-01, u_n= 0.733D-01

Figure 3.6: The time evolution of a drop deforming in a 2D extensional flow for $Ca = 0.05$ and $\lambda = 20$. The RK4 method is employed with $N_E = 6$, $N_B = 12$ and $\Delta t = 1 \times 10^{-4}$. The number of steps and the maximum normal velocity are denoted as N_{st} and u_n, respectively.

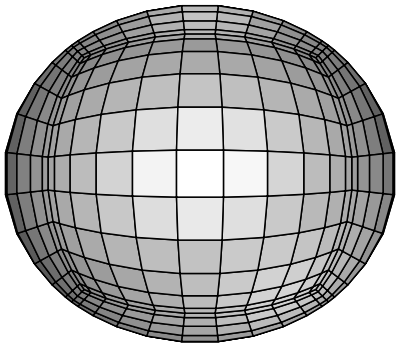

(a) N_{st}= 1000, time t= 0.100,

D= 0.742D-01, u_n= 0.482D-01

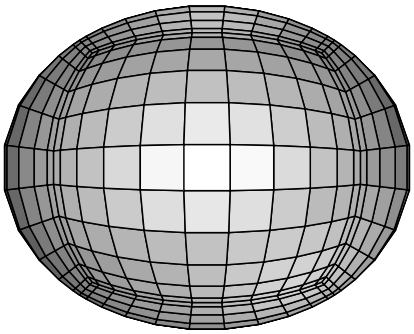

(b) N_{st}= 3000, time t= 0.300,

D= 0.115D+00, u_n= 0.990D-02

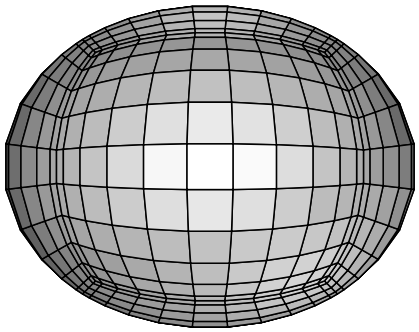

(c) N_{st}= 5000, time t= 0.500,

D= 0.122D+00, u_n= 0.222D-02

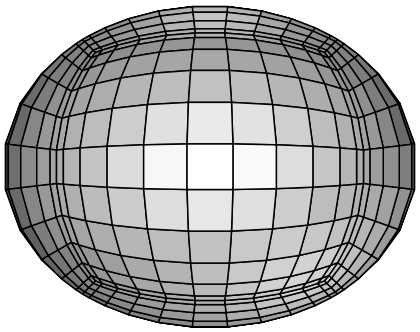

(d) N_{st}= 7000, time t= 0.700,

D= 0.124D+00, u_n= 0.516D-03

Figure 3.6: (continued) The time evolution of a drop deforming in a 2D extensional flow for $Ca = 0.05$ and $\lambda = 20$. The RK4 method is employed with $N_E = 6$, $N_B = 12$ and $\Delta t = 1 \times 10^{-4}$.

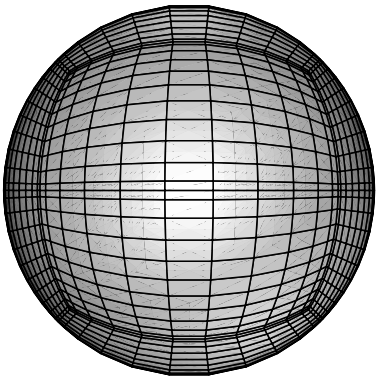

(a) N_{st}= 0, time t= 0.000,

D= 0.000D+00, u_n= 0.154D+01

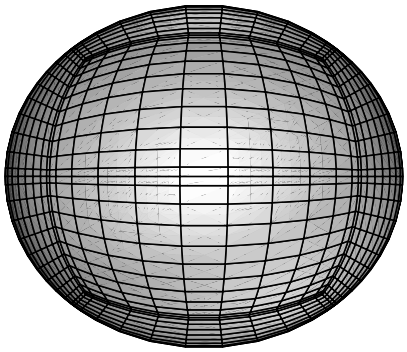

(b) N_{st}= 30, time t= 0.060,

D= 0.749D-01, u_n= 0.107D+01

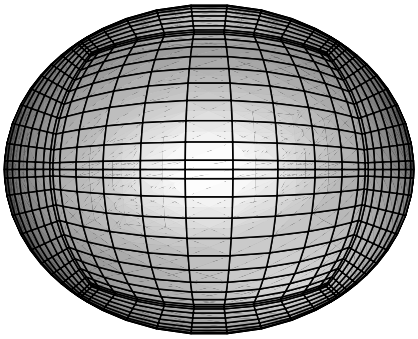

(c) N_{st}= 50, time t= 0.100,

D= 0.109D+00, u_n= 0.831D+00

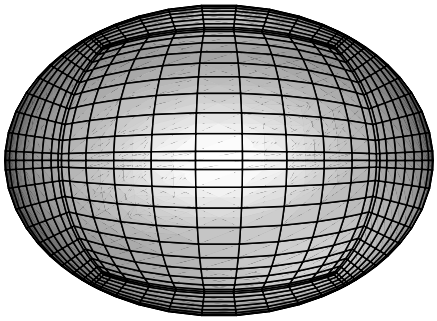

(d) N_{st}= 100, time t= 0.200,

D= 0.159D+00, u_n= 0.458D+00

Figure 3.7: The time evolution of a drop deforming in a 2D extensional flow for $Ca = 0.1$ and $\lambda = 0.1$. The RK4 method is employed with $N_E = 16$, $N_B = 12$ and $\Delta t = 2 \times 10^{-3}$.

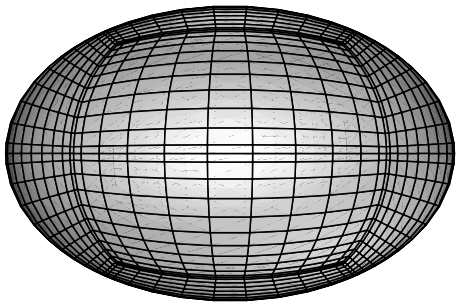

(a) N_{st}= 300, time t= 0.600,

D= 0.207D+00, u_n= 0.576D-01

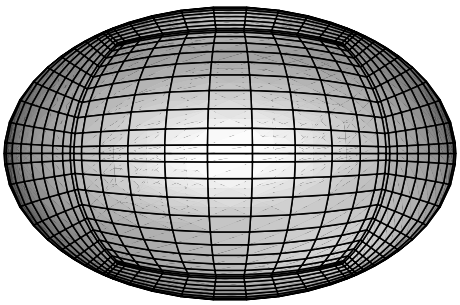

(b) N_{st}= 500, time t= 1.000,

D= 0.213D+00, u_n= 0.851D-02

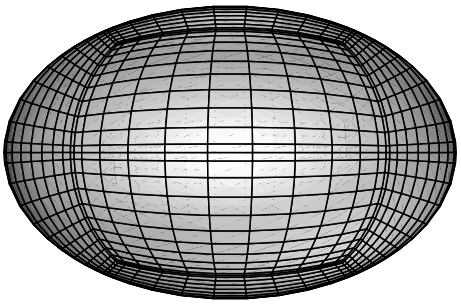

(c) N_{st}= 700, time t= 1.400,

D= 0.213D+00, u_n= 0.129D-02

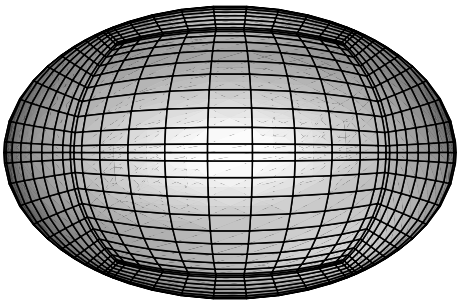

(d) N_{st}= 1000, time t= 2.000,

D= 0.214D+00, u_n= 0.106D-02

Figure 3.7: (continued) The time evolution of a drop deforming in a 2D extensional flow for $Ca = 0.1$ and $\lambda = 0.1$. The RK4 method is employed with $N_E = 16$, $N_B = 12$ and $\Delta t = 2 \times 10^{-3}$.

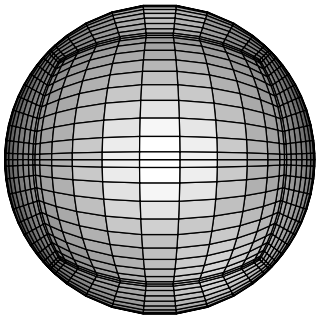

(a) N_{st}= 0, time t= 0.000,

D= 0.000D+00, u_n= 0.997D+00

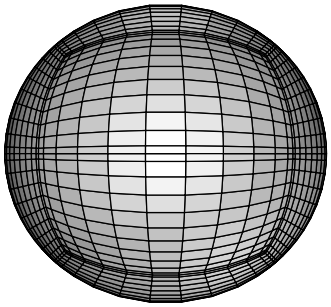

(b) N_{st}= 20, time t= 0.040,

D= 0.382D-01, u_n= 0.950D+00

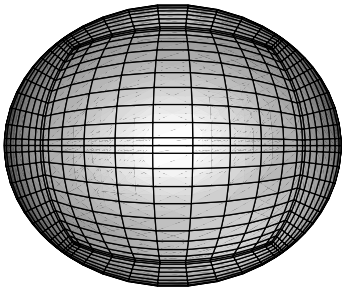

(c) N_{st}= 50, time t= 0.100,

D= 0.892D-01, u_n= 0.882D+00

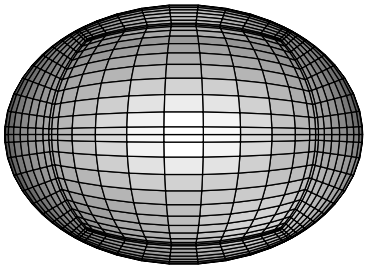

(d) N_{st}= 100, time t= 0.200,

D= 0.160D+00, u_n= 0.786D+00

Figure 3.8: The time evolution of a drop deforming in a 2D extensional flow for $Ca = 0.2$ and $\lambda = 1.0$. The RK4 method is employed with $N_E = 16$, $N_B = 12$ and $\Delta t = 2 \times 10^{-3}$.

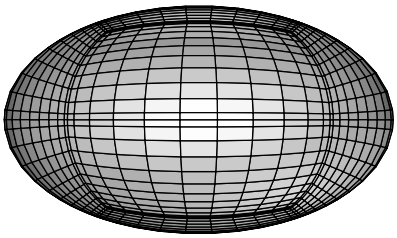

(a) N_{st}= 200, time t= 0.400,

D= 0.262D+00, u_n= 0.657D+00

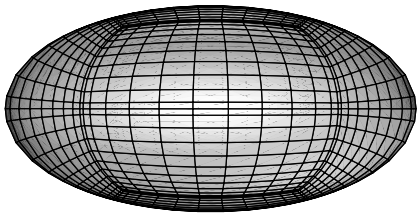

(b) N_{st}= 300, time t= 0.600,

D= 0.333D+00, u_n= 0.595D+00

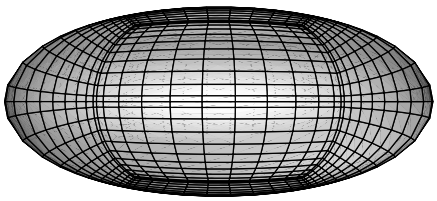

(c) N_{st}= 400, time t= 0.800,

D= 0.388D+00, u_n= 0.599D+00

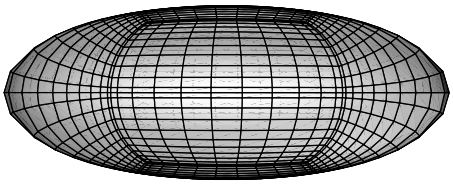

(d) N_{st}= 500, time t= 1.000,

D= 0.438D+00, u_n= 0.702D+00

Figure 3.8: (continued) The time evolution of a drop deforming in a 2D extensional flow for $Ca = 0.2$ and $\lambda = 1.0$. The RK4 method is employed with $N_E = 16$, $N_B = 12$ and $\Delta t = 2 \times 10^{-3}$.

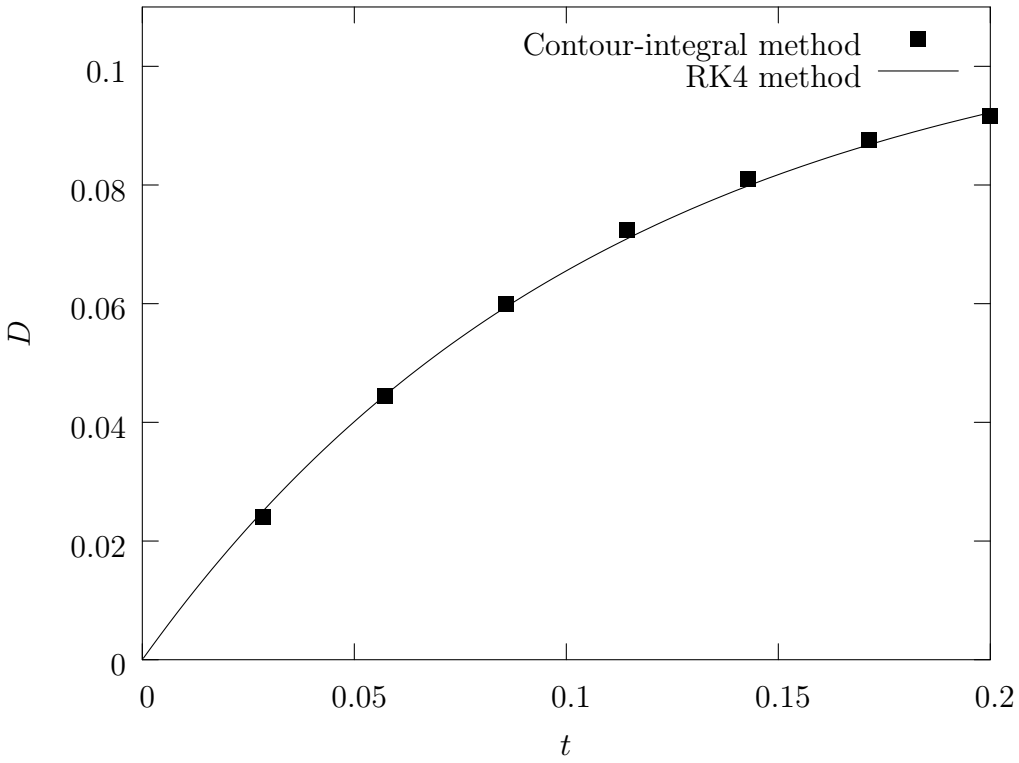

Figure 3.9: Comparison of our RK4 method with the contour-integral method from Ref.[1]: the drop deformation D versus time t for $Ca = 0.05$ and $\lambda = 1.0$. The boxes are taken from the figure 8 in Bazhlekov *et al.*[1]. The parameters in our computations are: $N_E = 6$, $N_B = 13$ and $\Delta t = 2.5 \times 10^{-4}$.

results of our study are compared with Taylor's predictions in table 3.2.

3.4.2 Imposed simple shear flow

For the droplet deformation in a simple shear flow with a shear rate G, the velocity far from the droplet is

$$\boldsymbol{u}^{\infty} = G \begin{pmatrix} 0 & 1 & 0 \\ 0 & 0 & 0 \\ 0 & 0 & 0 \end{pmatrix} \boldsymbol{x} = G\,(y, 0, 0) \tag{3.20}$$

2D extensional flow $\lambda = 0.9$				
Ca	D_E^{Newton}	D_E^{RK4}	u_n	Rel. Diff.
0.005	0.010891003	0.010890065	1.00D-04	8.61D-05
0.010	0.021799502	0.021797891	1.00D-04	7.39D-05
0.020	0.043740559	0.043738263	1.00D-04	5.25D-05
0.050	0.112028426	0.112033595	3.44D-04	4.61D-05

2D extensional flow $\lambda = 20$				
Ca	D_E^{Newton}	D_E^{RK4}	u_n	Rel. Diff.
0.005	0.011791166	0.011759178	3.38D-04	2.71D-03
0.010	0.023615590	0.023590620	1.43D-04	1.06D-03
0.020	0.047501627	0.047469273	1.00D-04	6.81D-04
0.050	0.124066113	0.123623951	5.16D-04	3.56D-03

Table 3.1: Comparison of the equilibrium deformation calculated by the Newton method D_E^{Newton} and the 4th-order Runge-Kutta (RK4) method D_E^{RK4} for a deforming droplet in a 2D extensional flow. The maximum normal velocity on the drop interface for the final step in the RK4 method is designated as u_n.

2D extensional flow $\lambda = 0.9$				
Ca	D_E^{Taylor}	D_E^{RK4}	u_n	Rel. Diff.
0.005	0.010888157	0.010890065	1.00D-04	1.75D-04
0.010	0.021776315	0.021797891	1.00D-04	9.91D-04
0.020	0.043552631	0.043738263	1.00D-04	4.26D-03
0.050	0.108881578	0.112033595	3.44D-04	2.89D-02

2D extensional flow $\lambda = 20$				
Ca	D_E^{Taylor}	D_E^{RK4}	u_n	Rel. Diff.
0.005	0.011785714	0.011759178	3.38D-04	2.25D-03
0.010	0.023571428	0.023590620	1.43D-04	1.06D-03
0.020	0.047142857	0.047469273	1.00D-04	6.92D-03
0.050	0.117857142	0.123623951	5.16D-04	4.89D-02

Table 3.2: Comparison of the equilibrium deformation calculated by Taylor's method D_E^{Taylor} and the RK4 method D_E^{RK4} for a deforming droplet in a 2D extensional flow. The maximum normal velocity on the drop interface for the final step in the RK4 method is designated as u_n.

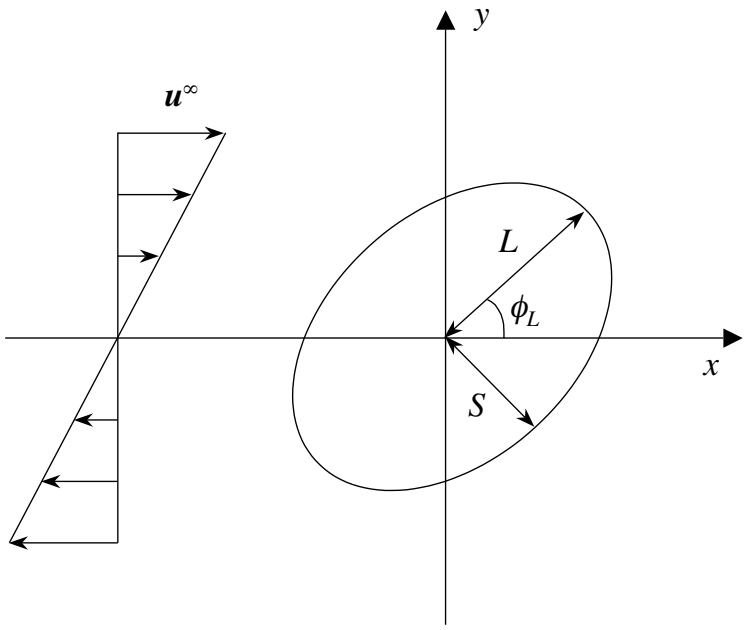

Figure 3.10: Illustration of a deforming drop in a simple shear flow.

while the lengths L in equation (3.4) form an angle ϕ_L with the x-axis when the droplet is deformed, as shown in figure 3.10.

The course of a small deformation ($Ca = 0.05$ and $\lambda = 20$) of the droplet in a simple shear flow is shown in figure 3.11. A larger deformation ($Ca = 0.24$ and $\lambda = 1.4$) is also demonstrated in figure 3.12. Figure 3.13 shows a large deformation with a super-critical capillary number $Ca = 1.0$ at a viscosity ratio $\lambda = 0.9$. For deformations in a simple shear flow, the droplet, which was first oriented at $\phi_L = 45°$, tends to rotate towards the x-axis as the deformation proceeds.

Experimental data for a large deformation in a simple shear flow with $Ca = 0.24$ and $\lambda = 1.4$ were made available by Guido and Villone[15]. Figure 3.14 shows a very good agreement between the experimental data and our computations.

A first-order analytical estimation of the equilibrium deformation D_E of a

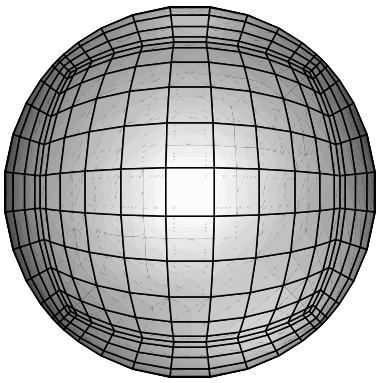

(a) N_{st}= 0, time t= 0.000,

D= 0.000D+00, u_n= 0.578D-01

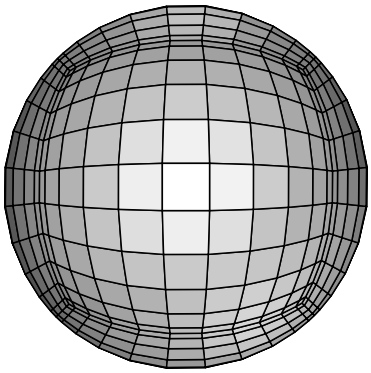

(b) N_{st}= 100, time t= 0.100,

D= 0.553D-02, u_n= 0.527D-01,

ϕ_L= 43.6°

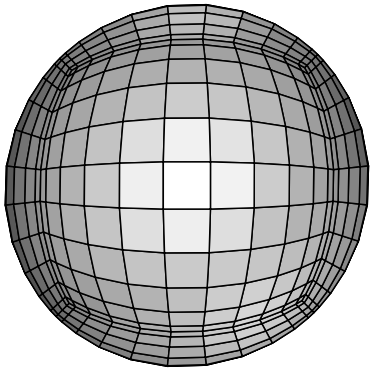

(c) N_{st}= 300, time t= 0.300,

D= 0.150D-01, u_n= 0.438D-01,

ϕ_L= 40.9°

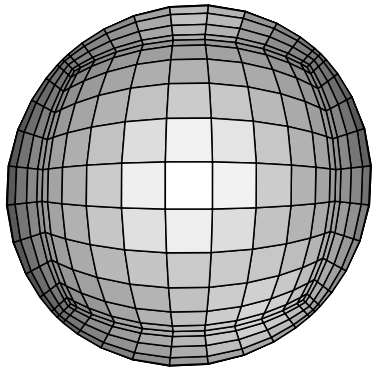

(d) N_{st}= 500, time t= 0.500,

D= 0.227D-01, u_n= 0.362D-01,

ϕ_L= 38.5°

Figure 3.11: The time evolution of a drop deforming in a simple shear flow for $Ca = 0.05$ and $\lambda = 20$. The RK4 method is employed with $N_E = 6$, $N_B = 12$ and $\Delta t = 1 \times 10^{-3}$. The orientation of the deformed drop is described by ϕ_L shown in figure 3.10.

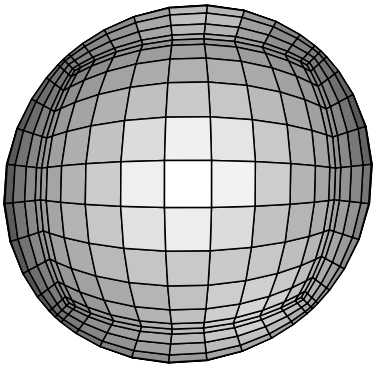

(a) N_{st}= 1000, time t= 1.000,
D= 0.356D-01, u_n= 0.226D-01,
ϕ_L= 33.2°

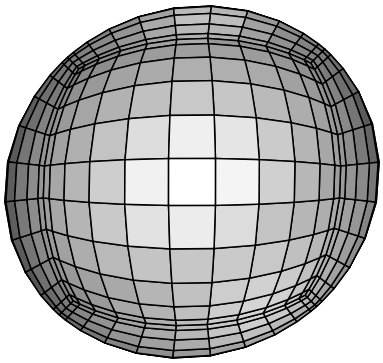

(b) N_{st}= 1500, time t= 1.500,
D= 0.420D-01, u_n= 0.137D-02,
ϕ_L= 29.2°

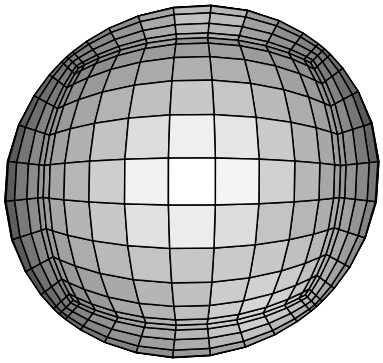

(c) N_{st}= 2000, time t= 2.000,
D= 0.446D-01, u_n= 0.809D-02,
ϕ_L= 26.4°

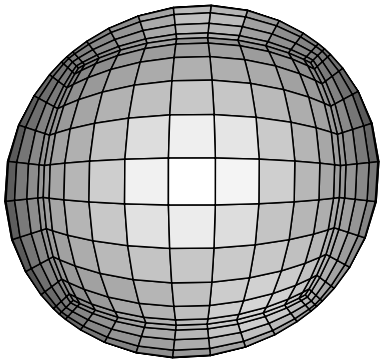

(d) N_{st}= 2500, time t= 2.500,
D=0.450D-01, u_n= 0.472D-02,
ϕ_L= 24.5°

Figure 3.11: (continued) The time evolution of a drop deforming in a simple shear flow for $Ca = 0.05$ and $\lambda = 20$. The RK4 method is employed with $N_E = 6$, $N_B = 12$ and $\Delta t = 1 \times 10^{-3}$.

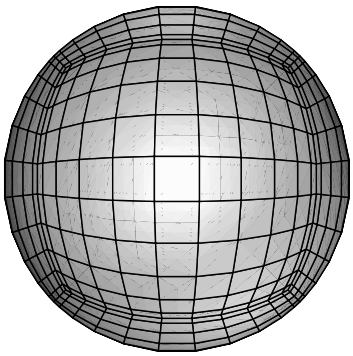

(a) N_{st}= 0, time t= 0.000,
D= 0.000D+00, u_n= 0.428D+00

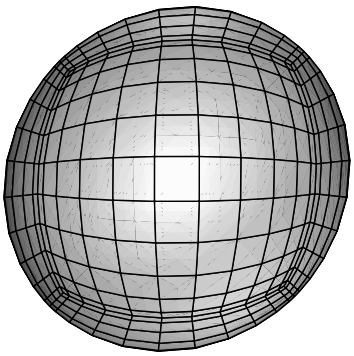

(b) N_{st}= 100, time t= 0.100,
D= 0.398D-01, u_n= 0.381D+00,
ϕ_L= 43.6°

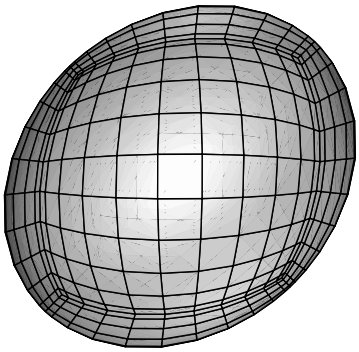

(c) N_{st}= 300, time t= 0.300,
D= 0.102D+00, u_n= 0.302D+00,
ϕ_L= 41.1°

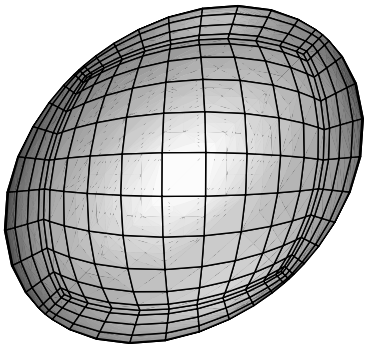

(d) N_{st}= 500, time t= 0.500,
D= 0.146D+00, u_n= 0.240D+00,
ϕ_L= 38.9°

Figure 3.12: The time evolution of a drop deforming in a simple shear flow for $Ca = 0.24$ and $\lambda = 1.4$. The RK4 method is employed with $N_E = 6$, $N_B = 12$ and $\Delta t = 1 \times 10^{-3}$.

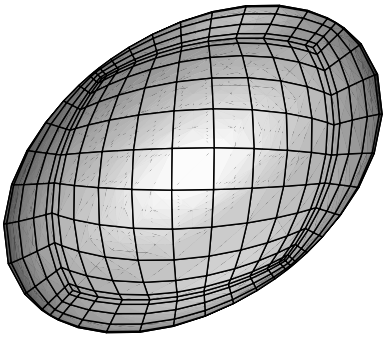

(a) $N_{st} = 1000$, time $t = 1.000$,
D= 0.211D+00, u_n= 0.142D+00,
ϕ_L= 34.8°

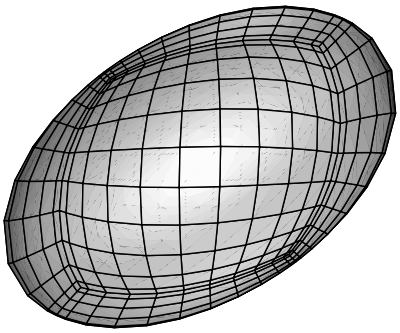

(b) $N_{st} = 1500$, time $t = 1.500$,
D= 0.240D+00, u_n= 0.814D-01,
ϕ_L= 32.2°

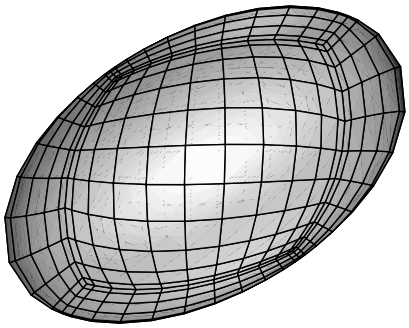

(c) $N_{st} = 2000$, time $t = 2.000$,
D= 0.254D+00, u_n= 0.473D-01,
ϕ_L= 30.6°

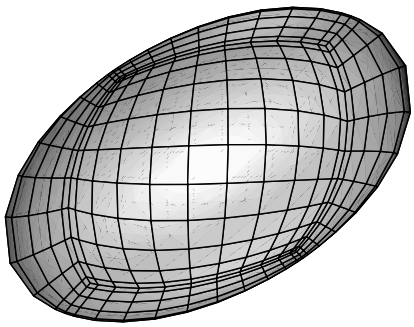

(d) $N_{st} = 2500$, time $t = 2.500$,
D= 0.261D+00, u_n= 0.270D-01,
ϕ_L= 29.7°

Figure 3.12: (continued) The time evolution of a drop deforming in a simple shear flow for $Ca = 0.24$ and $\lambda = 1.4$. The RK4 method is employed with $N_E = 6$, $N_B = 12$ and $\Delta t = 1 \times 10^{-3}$.

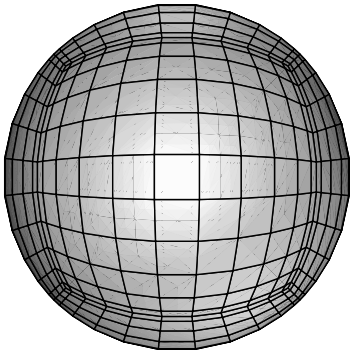

(a) N_{st}= 0, time t= 0.000,

D= 0.000D+00, u_n= 0.518D+00

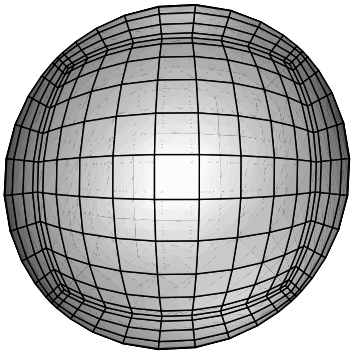

(b) N_{st}= 50, time t= 0.050,

D= 0.257D-01, u_n= 0.518D+00,

ϕ_L= 44.3°

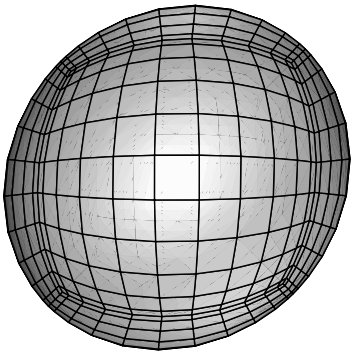

(c) N_{st}= 100, time t= 0.100,

D= 0.508D-01, u_n= 0.519D+00,

ϕ_L= 42.2°

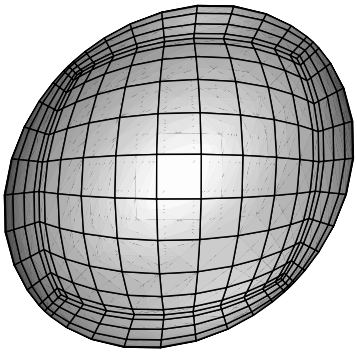

(d) N_{st}= 200, time t= 0.200,

D= 0.989D-01, u_n= 0.517D+00,

ϕ_L= 42.2°

Figure 3.13: The time evolution of a drop deforming in a simple shear flow for $Ca = 1.0$ and $\lambda = 0.9$. The RK4 method is employed with $N_E = 6$, $N_B = 12$ and $\Delta t = 1 \times 10^{-3}$.

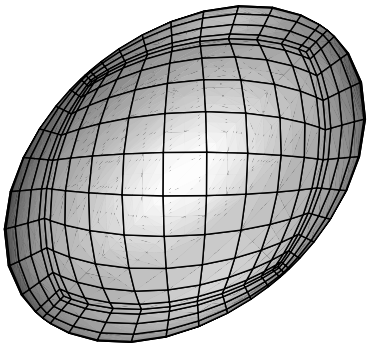

(a) N_{st}= 400, time t= 0.400,

D= 0.186D+00, u_n= 0.521D+00,

ϕ_L= 39.5°

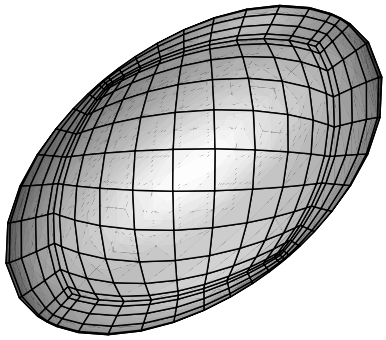

(b) N_{st}= 600, time t= 0.600,

D= 0.263D+00, u_n= 0.515D+00,

ϕ_L= 37.2°

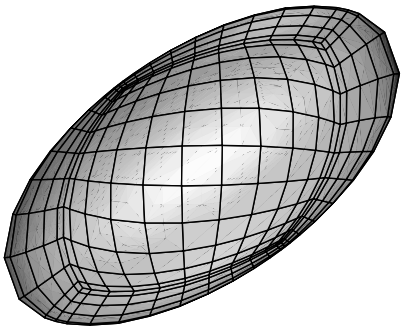

(c) N_{st}= 800, time t= 0.800,

D= 0.328D+00, u_n= 0.488D+00,

ϕ_L= 35.2°

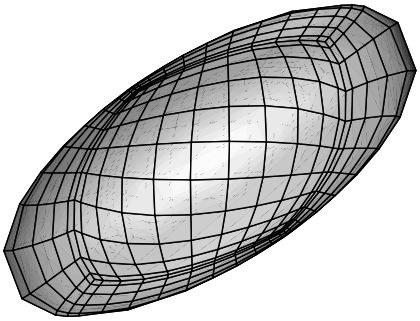

(d) N_{st}= 1000, time t=1.000,

D= 0.384D+00, u_n= 0.447D+00,

ϕ_L= 33.2°

Figure 3.13: (continued) The time evolution of a drop deforming in a simple shear flow for $Ca = 1.0$ and $\lambda = 0.9$. The RK4 method is employed with $N_E = 6$, $N_B = 12$ and $\Delta t = 1 \times 10^{-3}$.

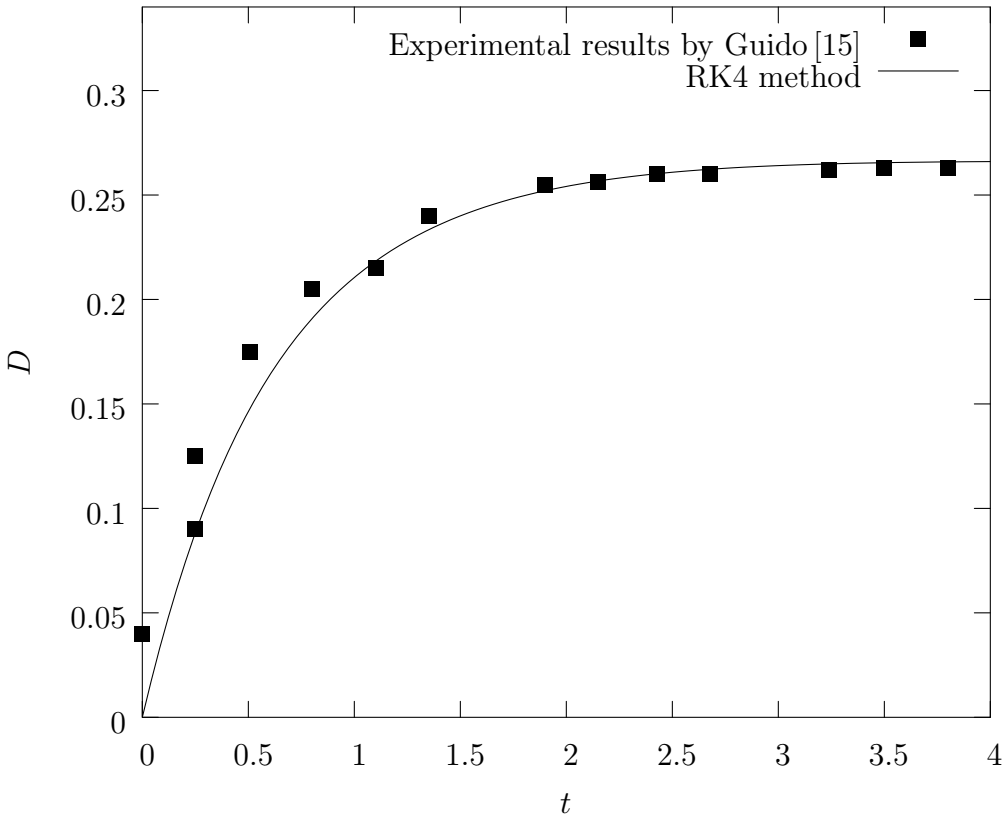

Figure 3.14: Comparison of our RK4 method with experimental results from Ref.[15]: the drop deformation D versus time t for $Ca = 0.24$ and $\lambda = 1.4$. The boxes are taken from the figure 6 in Guido and Villone[15]. The parameters in our computations are: $N_E = 6$, $N_B = 12$ and $\Delta t = 1.0 \times 10^{-3}$.

droplet in an imposed simple shear flow was first derived by Taylor[34],

$$D = Ca \frac{19\lambda + 16}{16\lambda + 16} \tag{3.21}$$

This relation is valid for small deformations only. The numerical results of our study are compared with Taylor's predictions in table 3.3.

Simple shear flow $\lambda = 0.9$				
Ca	D_E^{Taylor}	D_E^{RK4}	u_n	Rel. Diff.
0.005	0.005444079	0.00544311368	1.01D-04	1.73D-04
0.010	0.010888158	0.01088672207	1.00D-04	1.31D-04
0.020	0.021776312	0.02177716906	1.00D-04	3.94D-05
0.050	0.054440789	0.05450853227	1.68D-04	1.24D-03

Table 3.3: Comparison of the equilibrium deformation calculated by Taylor's method D_E^{Taylor} and our RK4 method D_E^{RK4} for a deforming droplet in a simple shear flow. The maximum normal velocity on the interface of the drop for the final step in the RK4 method is designated as u_n.

3.5 Selection of the time step

In order to maintain the stability of numerical calculations for any explicit time-integration algorithm, a small enough time step has to be selected. Table 3.4 demonstrates various criteria for the selection of the time step from different studies.

The current study quantitatively investigates the maximum time step Δt_{max} under which the stability of our numerical scheme is maintained. Table 3.5 lists Δt_{max} for different capillary numbers Ca and viscosity ratios λ, for the number of basis points N_B varying from 9 to 13 when $N_E = 6$. We conclude that for a given viscosity ratio λ and a fixed number of elements N_E, the maximum time step is given by

$$\Delta t_{max} \sim Ca\, \Delta x \tag{3.22}$$

Authors	Δt	Notes
Zinchenko[38]	$\frac{0.1}{G}$	Initial Δt varies
Navot[21]	$\sim \Delta x$	
Rallison[25]	$\leq K\Delta x$	K = constant of $O(1)$
Loewenberg[19]	$\leq K\Delta x$	K = constant of $O(1)$
Bazhlekov[1]	$< O(Ca \cdot min(\Delta x))$	
Cristini[4]	$< \frac{\mu \Delta x_{min}}{\gamma}$	
Roumeliotis[30]	$= \frac{\Delta x_{max}}{max_i\|\upsilon(\xi_i)\|}$	$\upsilon(\xi_i)$: velocity of node ξ_i

Table 3.4: Summary of the time step criteria used in different studies.

where Δx is the grid size. All the computations conducted in this chapter satisfy this criterion.

3.6 Convergence with decreasing grid size

To determine the convergence of our method, the droplet deformation has been calculated for different grid sizes by changing the number of basis points N_B on each spectral element for several physical problems. These tests show similar behavior with the one presented in table 3.6 for a 2D extensional flow with $Ca = 0.05$ and $\lambda = 20$. These tests show that with increasing N_B, i.e., decreasing grid size, the calculated droplet deformation D achieves an spectral (i.e., exponential) convergence and verify that our method is a high-order/high-accuracy method.

	$\lambda = 0.9$		$\lambda = 20$	
N_B	$Ca = 0.05$	$Ca = 0.005$	$Ca = 0.05$	$Ca = 0.005$
9	0.8D-02	0.8D-03	0.9D-01	0.9D-02
10	0.5D-02	0.4D-03	0.5D-01	0.6D-02
11	0.3D-02	0.3D-03	0.3D-01	0.4D-02
12	0.2D-02	0.2D-03	0.2D-01	0.3D-02
13	0.1D-02	0.1D-03	0.1D-01	0.2D-02

Table 3.5: The maximum time step Δt_{max} for different λ, Ca and N_B found by employing our RK4 algorithm.

N_B	D	Error
8	0.1107075548D-01	2.0D-06
10	0.1107273956D-01	4.9D-08
12	0.1107278740D-01	1.3D-10
14	0.1107278872D-01	0

Table 3.6: Exponential convergence in deformation D by increasing the number of basis points N_B. The droplet deforms in a 2D extensional flow for $Ca = 0.05$ and $\lambda = 20$. The deformation D is shown for time $t = 0.1$. The time step is $\Delta t = 1 \times 10^{-4}$. The number of elements is $N_E = 6$.

Chapter 4

Stokes Flow Over a Hump in a Microtube

As described in Chapter 1, the study on the flow over a hump in microtubes is interested in many areas. In physiological systems, the shear stress distribution, total force and torque exerted on the cell surface play a pivotal role in the mechanotransduction phenomena (which involve the relation between the hemodynamic shear force received by endothelial cells and the chemical signals they send out) as well as the leukocyte/endothelial cell adhesion in blood flow[14]. From the viewpoint of industrial applications such as coating and deposition, the shear stress on the protuberance in a micro-channel may affect the the mass transfer near the protuberance[17]. In this chapter, we investigate the behavior of the shear stress, total force and torque on the protuberance/cell attached to a cylindrical microtube wall. This is the first time that a three-dimensional cylindrical model is employed.

4.1 Configuration of the geometry

The Boundary Element Method described in Chapter 2 has demonstrated its robustness, stability and accuracy earlier in numerous applications by Muldowney and Higdon[18, 20], and Dimitrakopoulos and Higdon[7, 8, 10, 11, 12]. In this study, the

method is employed in the analysis of the fluid force exerted on the protuberance in a microtube.

The geometry of the tube is illustrated in figure 4.1. The spherical cap represents a spreading cell or a protuberance attached to the inner wall of the tube. The protuberance is assumed to be a part of a sphere with radius a. The radius of the cylindrical tube is denoted as R, and the half length of the tube is designated as L. The angle θ controls the degree of which the hump blocks the flow in the tube. If the hump represents a spreading cell, the angle θ can also be interpreted as the contact angle. In contrast to the spherical protuberance on a flat surface, the angle θ along the contact line of the hump on a cylindrical surface is a function of the azimuthal angle ϕ, as shown in figure 4.2. The contact angle θ always shows a maximum at $\phi = 90°$. For a given aspect ratio a/R, the relationship between the contact angle θ and the azimuthal angle ϕ is determined by the contact angle θ_0 at $\phi = 0°$.

The surface of the tube and the protuberance is composed of $N_E = 39$ elements with $N_B \times N_B$ spectral points (for details, see section 2.5). A global view of the discretization of the cylinder body and the hump is shown in figure 4.3(a). The discretization of the end lids of the cylinder is displayed in figure 4.3(b). Figure 4.3(c) shows the bottom view of the system. The surface area on the protuberance is labeled as S_1. It is composed of 5 elements generated by a cube projection when the contact angle θ_0 is less than 90°. If the contact angle $\theta_0 > 90°$, 9 elements are employed. The immediate vicinity of the hump on the cylinder (area S_2) experiences an acute jump in the shear stress. In order to achieve a sufficient accuracy in this

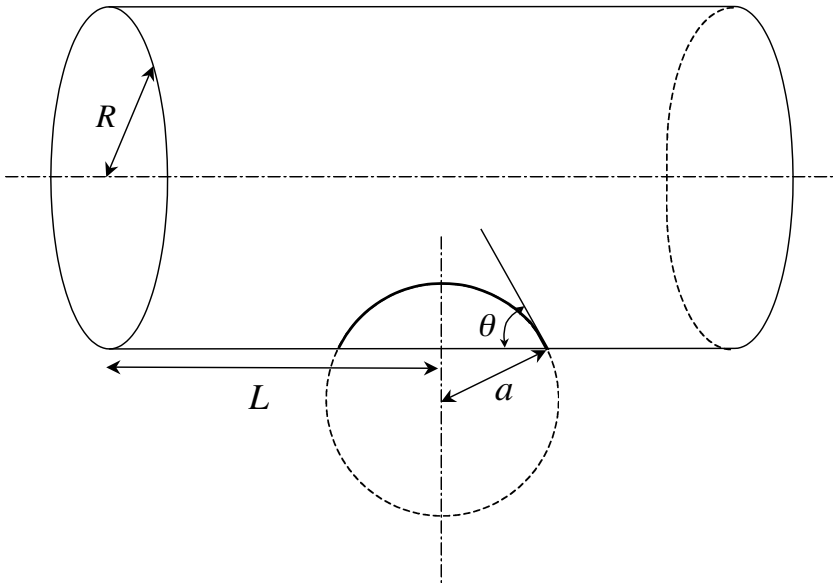

Figure 4.1: Illustration for the geometry.

area, 16 elements are applied. The area S_2 has a width $d = 0.5r_0$, where r_0 is defined as half the distance between the intersection of the hump and the cylinder in XZ plane. The cylinder surface above the hump is designated as S_3. The cylindrical body (area S_4) is divided into three rows (L_1, L_2 and L_3) shown in figure 4.3(c). In order to capture the change in shear stress on the cylinder surface near the hump and to maintain the accuracy of the solution, the length of the first row L_1 is set to be equal to r_0 and the length of the second row L_2 is set to be $2r_0$. The length of the third row L_3 is decided by the length L which will be discussed later.

In figure 4.4, the division of the entire geometry into elements is illustrated by projecting onto the XY plane. The elements 1 to 5 belong to the hump (S_1), the

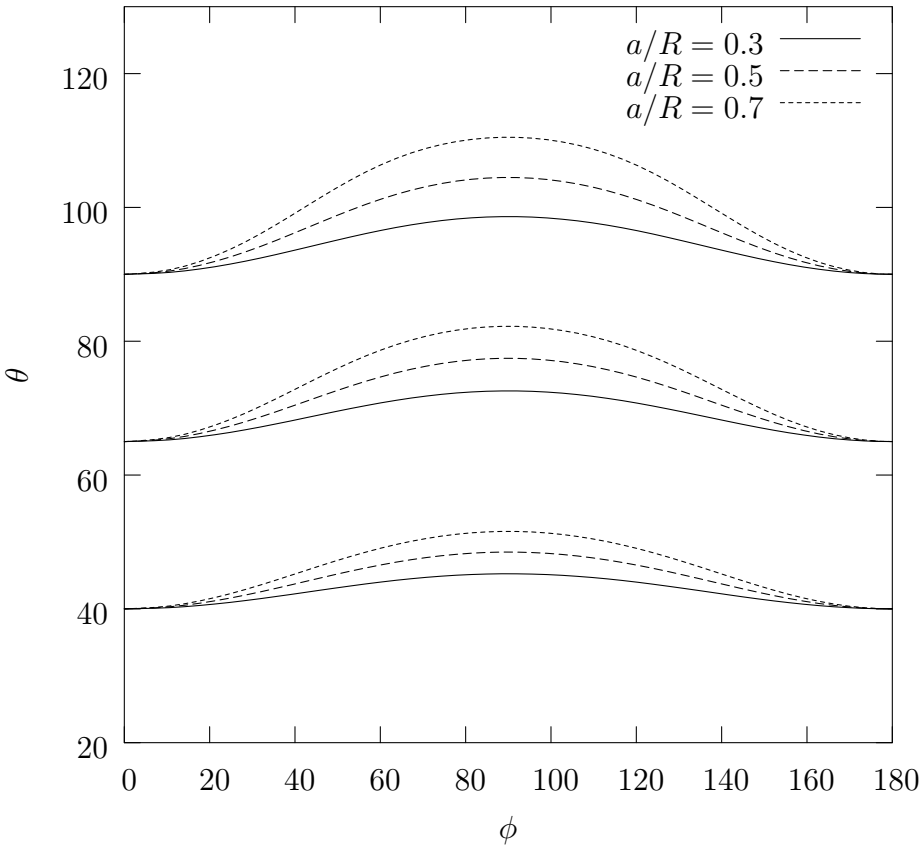

Figure 4.2: The contact angle θ is plotted against the azimuthal angle ϕ for $a/R = 0.3, 0.5, 0.7$. The initial contact angle $\theta_0 = 40°, 65°, 90°$.

elements 6 to 21 distribute on the immediate vicinity of the hump on the cylinder (S_2), the elements 22 to 35 represent the rest area (S_3 and S_4) on the cylinder body, and the elements 36 to 39 are the four elements on the circular lids of the cylinder shown in figure 4.3(b). They finalize the entire model as a closed system to facilitate applying the governing BIE (2.3). The two lids are fluid boundaries with a velocity profile of a Poiseuille flow.

In order to determine a sufficient number of basis points N_B on each element and to test the validity of the element distribution on the boundary surface, a

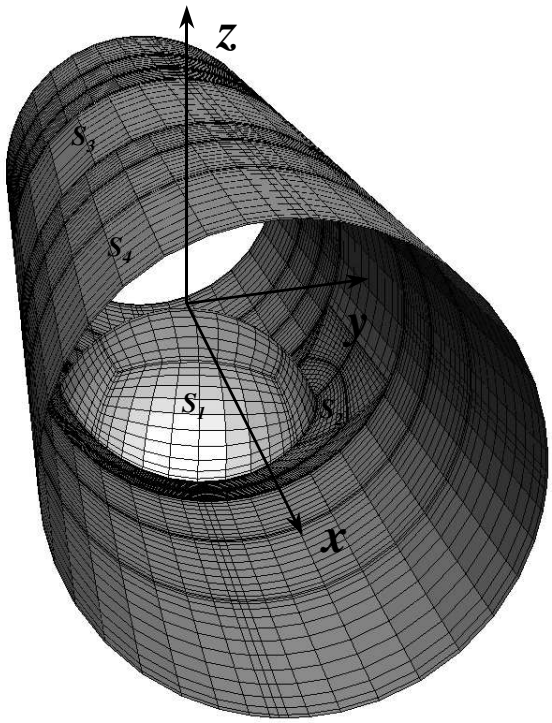

(a)

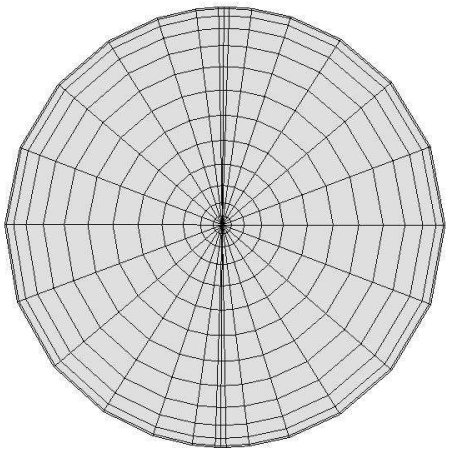

(b)

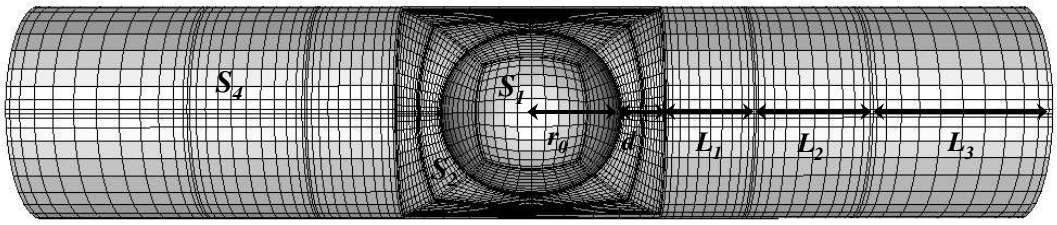

(c)

Figure 4.3: Configuration of geometry: (a) overall illustration of the system; (b) configuration of the circular "lids" at the end of the cylindrical tube; (c) bottom view for of the entire system.

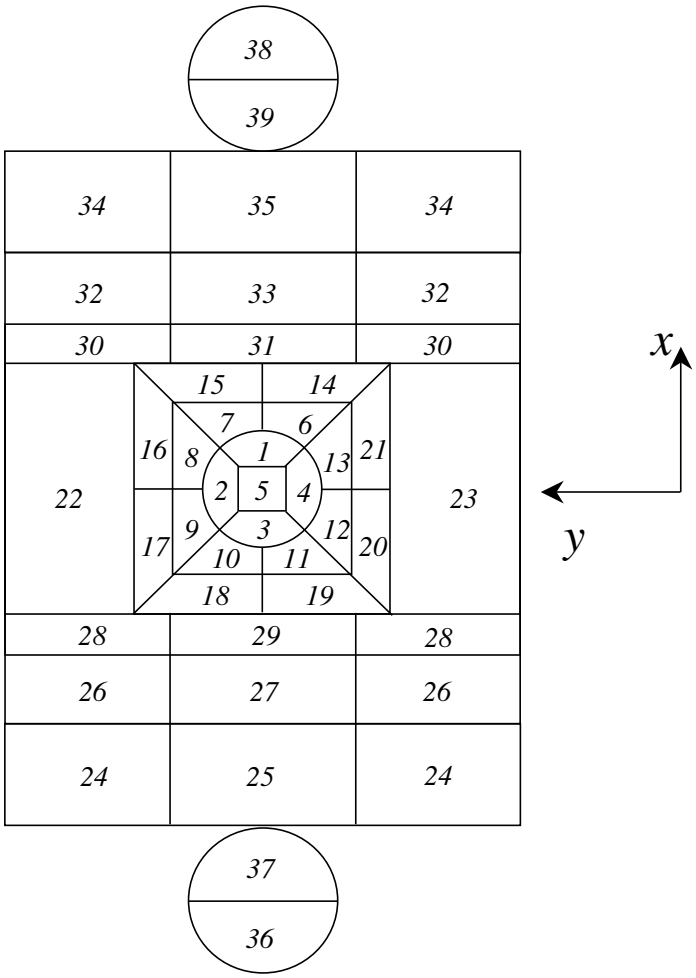

Figure 4.4: Illustration for the element distribution (expanded cylindrical surface).

	$a/R = 0.25$		$a/R = 0.33$	
N_B	$\theta_0 = 90°$	$\theta_0 = 70°$	$\theta_0 = 90°$	$\theta_0 = 70°$
6	0.032	0.030	0.049	0.044
7	0.0016	0.0014	0.0019	0.0014
8	0.0014	0.0013	0.0018	0.0018
9	0.00016	0.00015	0.00021	0.00021
10	0.00013	0.00012	0.00017	0.00015
11	0.000021	0.000018	0.000027	0.000023

Table 4.1: Maximum quadrature error with increasing number of basis points N_B.

quadrature test of an imaginary fluid boundary in an undisturbed Poiseuille flow has been performed. Four combinations of geometric parameters have been tested: $a/R = 0.25, 0.33$ and $\theta_0 = 90°, 70°$. The number of polynomial basis points N_B ranges from 6 to 11 and an exponential decay of the maximum error is witnessed, as shown in table 4.1. Based on these results, N_B=9 is chosen as the number of basis points, which produces a maximum error in the order of 10^{-4}. Tests for the actual physical variables were also conducted and a similar convergence was found.

It is assumed that there is no disturbance on the fluid boundary of the circular lids of the tube if they are far enough from the hump. Practically, a finite tube length has to be chosen in our numerical method. To determine the sufficient length, we calculate the total force F_x exerted on the surface of the hump with the half length of the cylinder L varying from 3 to 35 times the radius of the cylinder R. As shown

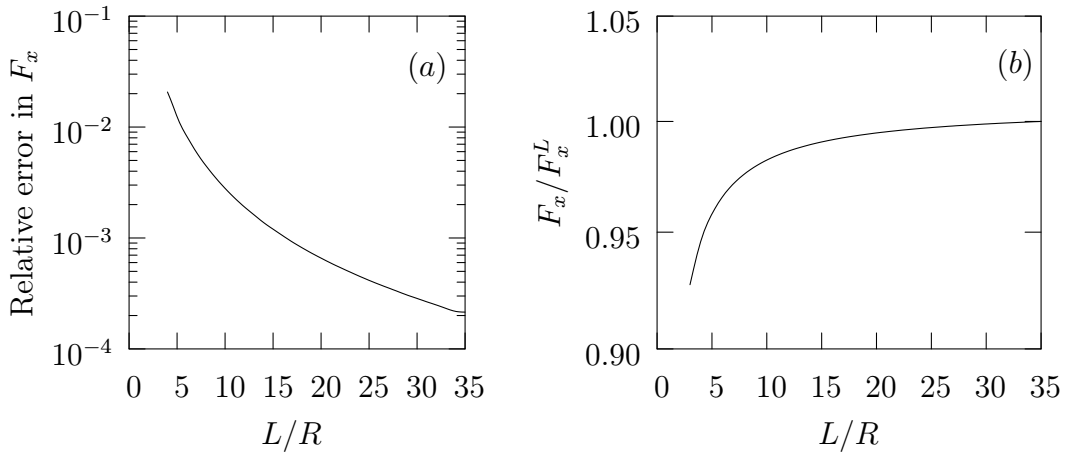

Figure 4.5: The asymptotic relationship for the force exerted on the hump with respect to the half length L of the cylinder: (a) the relative error in F_x versus the length L; (b) the aspect ratio F_x/F_x^L versus the length L, where F_x is the x-component of the force exerted on the protuberance and F_x^L is the same quantity for $L = 35R$.

in figure 4.5, when the tube length increases, the total force F_x on the protuberance increases and reaches an asymptotic limit $F_x/F_x^L = 1.0$, where F_x^L is the total force on the protuberance for $L = 35R$ and is assumed to be the "exact" value of the force. The result shows that the aspect ratio $L/R = 23$ is sufficient to produce a relative error of 5×10^{-4} in the force. Additional tests on the maximum shear stress and the torque on the hump have been performed with similar results. As a consequence, the aspect ratio $L/R = 23$ is chosen for the computations in this study.

4.2 Physical variables and dimensionless analysis

The shear stress τ, the total force F_x and the torque T_y on the protuberance are the physical variables we study in this work. They are defined by

$$\tau = \sqrt{(f_x^L)^2 + (f_y^L)^2} \tag{4.1}$$

$$F_x = \int_{hump} f_x \, dS \tag{4.2}$$

$$T_y = \int_{hump} (\boldsymbol{l} \times \boldsymbol{f})_y \, dS \tag{4.3}$$

where $\boldsymbol{f}$ is the force vector calculated from the governing BIE (2.3), while f_x^L and f_y^L are the two tangent components of the force. The vector $\boldsymbol{l}$ is the distance between the attachment center of the hump and the hump surface. Due to the symmetry, the rest components of the total force and the torque, F_y, F_z, T_x and T_z, are identically zero.

We use the shear stress on the tube wall far from the protuberance τ_{wall}^{∞} as the scale for the shear stress τ. It is given by

$$\tau_{wall}^{\infty} = \tau_{rx}|_{r=R} = \frac{2\,\mu\,u_{max}^{\infty}}{R} \tag{4.4}$$

where μ is the viscosity of the fluid and u_{max}^{∞} is the maximum velocity far from the hump. The tube radius R is used as the length scale. The maximum velocity u_{max}^{∞} is also the scale for the flow velocity. The ratio $\tau/\tau_{wall}^{\infty}$ physically demonstrates the amplification in the shear stress caused by the protuberance. From equation (4.2), $F_x \sim R^2 \boldsymbol{f} \sim R^2\,\tau_{wall}^{\infty}$. From equation (4.3), $T_y \sim R^3 \boldsymbol{f} \sim R^3\,\tau_{wall}^{\infty}$. As a summary, in this chapter we choose R, u_{max}^{∞}, τ_{wall}^{∞}, $R^2\,\tau_{wall}^{\infty}$ and $R^3\,\tau_{wall}^{\infty}$ as the scales for the length, flow velocity, shear stress, force and torque, respectively.

4.3 Results and discussion

In this section we investigate the stress field on the protuberance and its vicinity area influenced by the flow in the microtube. We first describe the two geometric parameters in our system: the characteristic length of the hump $\tilde{a}$ and the contact angle θ_0. We then examine the distribution of the shear stress over the hump and the maximum shear stress which is always located on the peak of the hump. Finally, we determine the total force and torque on the hump and demonstrate their behavior as functions of the two geometric parameters.

We define the characteristic length of the protuberance $\tilde{a}$ by

$$\tilde{a} = \left(\frac{3V}{4\pi}\right)^{1/3} \tag{4.5}$$

where V is the volume of the protuberance/cell attached on the cylindrical wall. Thus, the length $\tilde{a}$ reflects the volume of protuberance blocking the tube flow. In addition, the other independent geometric parameter, the contact angle θ_0, describes the way the protuberance/cell spreads on the tube surface. If the length $\tilde{a}$ (or the volume V) of the hump varies with a fixed contact angle θ_0, this is equivalent to changing the radius a of the spherical cap, as shown in figure 4.6(a). On the other hand, varying the contact angle θ_0 with a fixed volume is a combination of varying θ_0 and a, as shown in figure 4.6(b).

The shear stress over the hump and its nearby area is shown in figure 4.7. This figure demonstrates the shear stress as arrows starting from each discretized point on the surface. The length of the arrows shows the magnitude of the shear stress.

Figure 4.8 shows the distribution of the shear stress τ as a function of the arc

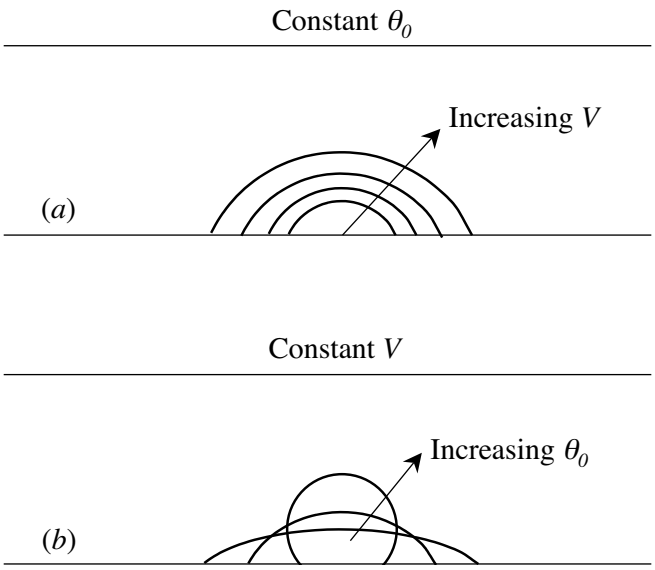

Figure 4.6: Description of the variation of two geometric parameters of the current problem: (a) increase the hump volume V while θ_0 is constant; (b) increase the contact angle θ_0 while the volume V is constant.

length s along the intersection of the hump surface with the XZ plane ($y = 0$) for different hump volumes. The contact angle θ_0 is fixed to be 90°. The original point of the arc length s is set at the center of the hump surface. The arc length is also normalized as $\tilde{s} = s/(a\pi)$, where $a\pi$ is half the circumference of the circle shown in figure 4.1. Figure 4.9 shows the relationship between the shear stress and the arc length along the intersection of the hump surface with the YZ plane ($x = 0$).

These results show that the shear stress distribution has been greatly influenced by the existence of the hump. The stress on the upper part of the hump is much larger than that on the cylinder wall. This is due to the redistribution of the flow field when the tube suddenly shrinks because of the hump. The maximum

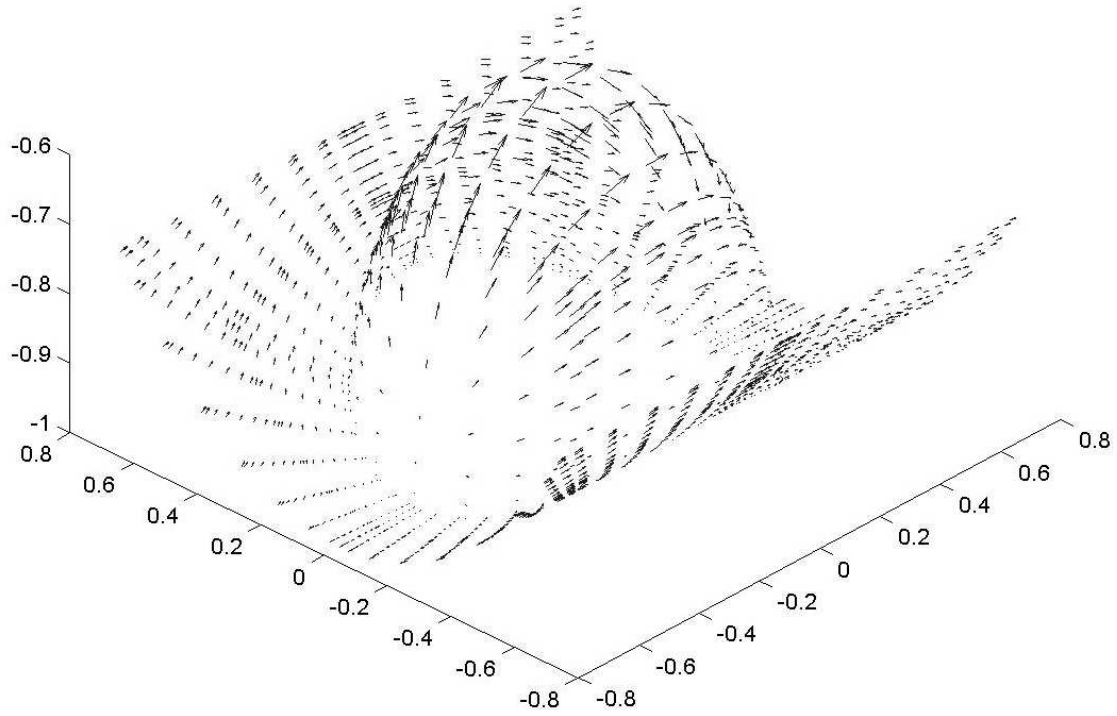

Figure 4.7: A three-dimensional arrow plot for the shear stress on the hump and its nearby area. The aspect ratio $\tilde{a}/R = 0.38$ and the contact angle $\theta_0 = 90°$.

shear stress always appears at the peak of the hump due to symmetry. On the lower part of the hump and its neighbor area on the cylinder wall, the shear stress is found to be smaller than the shear stress exerted on the cylinder wall far away and even approaches zero at a certain position. As explained in Higdon[17] and Pozrikidis[23], this phenomenon is caused by the presence of the Moffat eddies (i.e., a weak recirculating flow) near the corner where the bump and the cylinder meet. The influence of the hump ranges from the center of the cell to several hump radii (i.e., $s \approx 1.5\, a\pi$).

Figure 4.8 and figure 4.9 also indicate that for small hump volumes, an increase

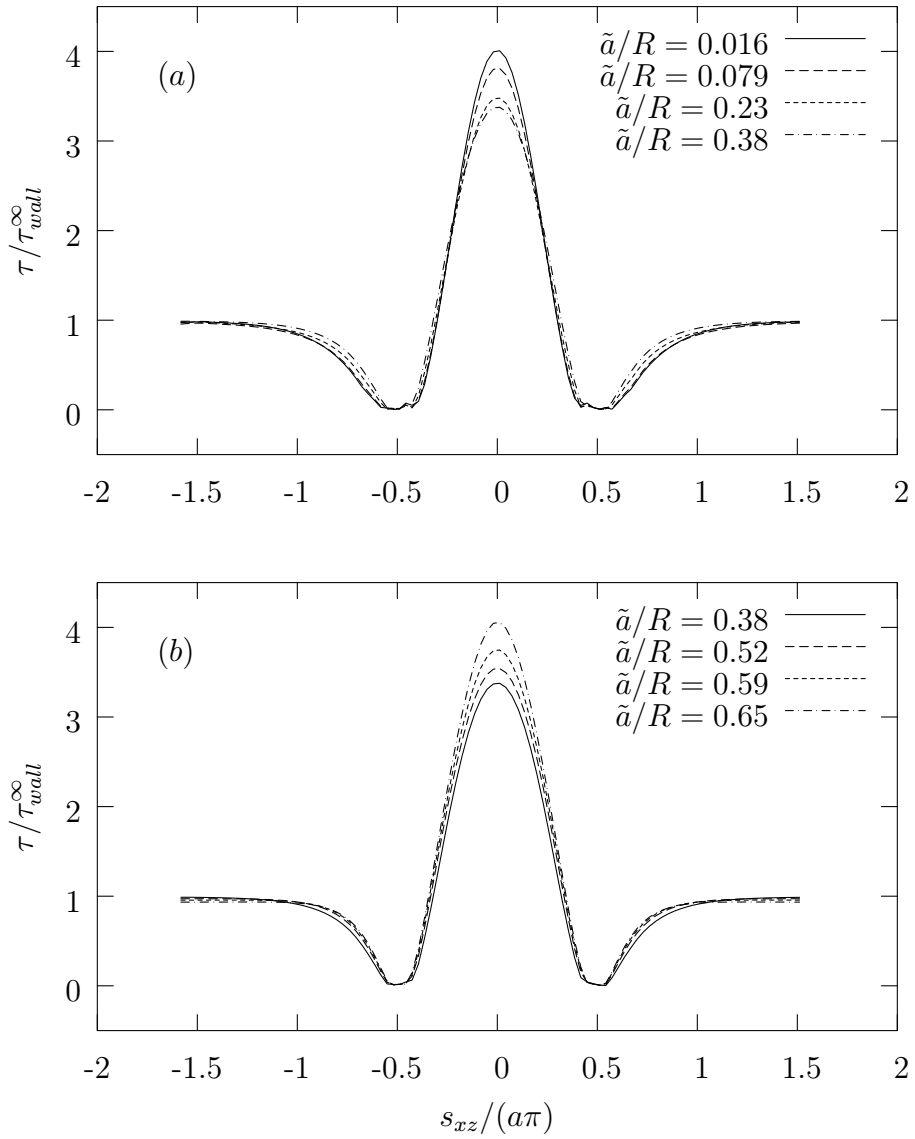

Figure 4.8: The shear stress distribution on the surface of a hump spreading axisymmetrically on the inner surface of a cylindrical tube. The shear stress is plotted as a function of the arc length $s_{xz}/(a\pi)$ at the intersection of the hump surface with the XZ plane. The contact angle $\theta_0 = 90°$. (a) The values of $\tilde{a}/R$ shown correspond to $a/R = 0.02, 0.1, 0.3, 0.5$. (b) The values of $\tilde{a}/R$ shown correspond to $a/R = 0.5, 0.7, 0.8, 0.9$. The wall shear stress far from the hump is denoted as τ^{∞}_{wall}.

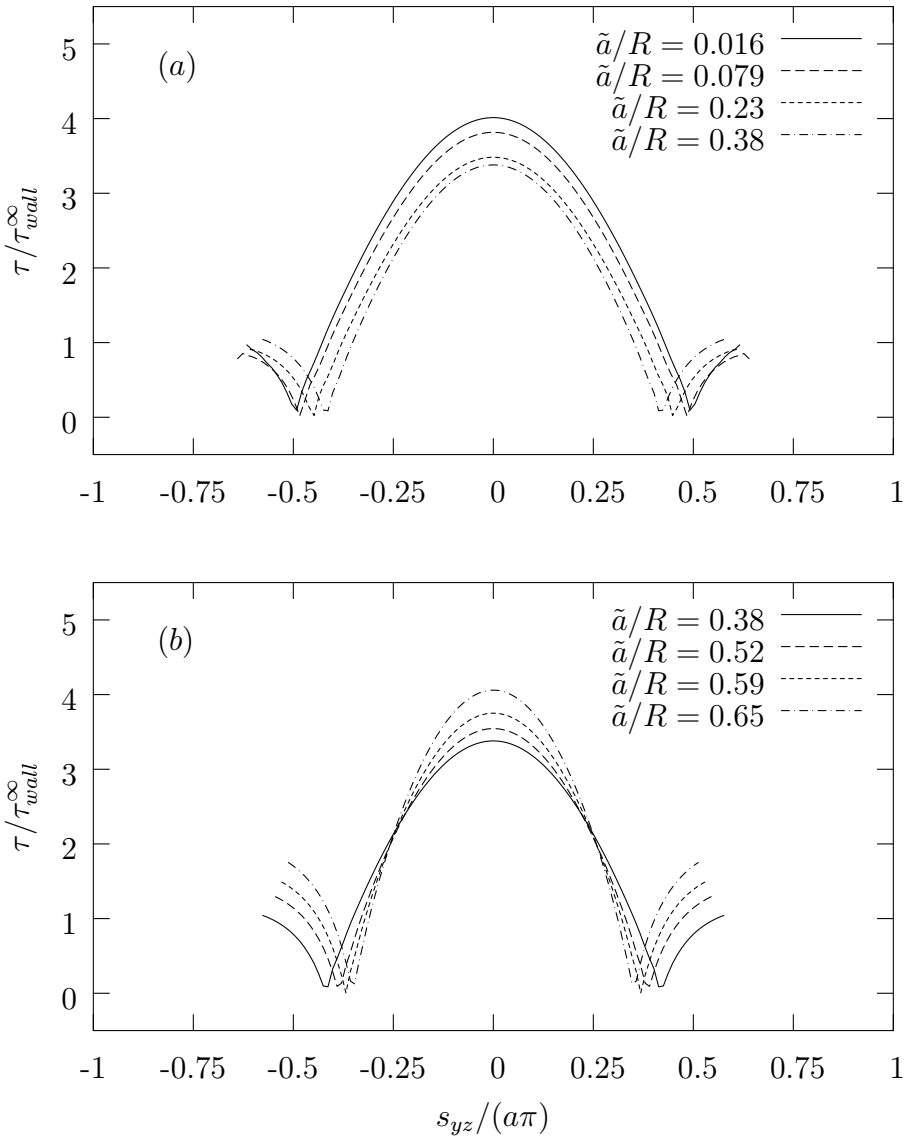

Figure 4.9: The shear stress distribution on the surface of a hump spreading axisymmetrically on the inner surface of a cylindrical tube. The shear stress is plotted as a function of the arc length $s_{yz}/(a\pi)$ at the intersection of the hump surface with the YZ plane. The contact angle $\theta_0 = 90°$. (a) The values of $\tilde{a}/R$ shown correspond to $a/R = 0.02, 0.1, 0.3, 0.5$. (b) The values of $\tilde{a}/R$ shown correspond to $a/R = 0.5, 0.7, 0.8, 0.9$. The wall shear stress far from the hump is denoted as τ^{∞}_{wall}.

in the hump volume results in a decreasing maximum shear stress, while for large hump volumes, the maximum shear stress increases with the hump volume. Thus, the maximum shear stress reaches a minimum at $\tilde{a}/R \approx 0.38$. A more comprehensive plot, figure 4.10, demonstrates the change of the maximum shear stress with the hump characteristic length $\tilde{a}$ for the contact angle θ_0 varying from 30° to 120°. This figure shows that for a given angle θ_0 the shear stress at the hump peak reaches a minimum at $\tilde{a}/R \approx 0.38$. For large hump volumes, the maximum shear stress τ^{max} increases with the hump volume; this increase is more dramatic for large angles θ_0. For small humps, τ^{max} slightly decreases as the hump volume increases. When the hump volume is constant, the maximum shear stress increases monotonically with the contact angle θ_0.

The angle θ_0 also influences the shear stress distribution over the entire hump and its nearby region. Figure 4.11 demonstrates the behavior of the shear stress $\tau/\tau^{\infty}_{wall}$ as a function of the arc length $s/(a\pi)$ for different contact angles θ_0 on the intersections of the hump with the XZ and YZ plane. The characteristic length of the hump is $\tilde{a}/R = 0.30$. This figure shows that by increasing the contact angle θ_0, the shear stress is greatly increased everywhere on the hump due to the corresponding increase of the blocking.

We now consider the extreme case when the aspect ratio $\tilde{a}/R$ is as small as 0.016, i.e., the radius of the cylinder is much larger than the size of the protuberance. Due to the extremely small size of the hump, the parabolic flow inside the tube can be considered as a simple shear flow near the hump, while the curvature of the cylindrical tube can be neglected. Therefore, the results of our computations are

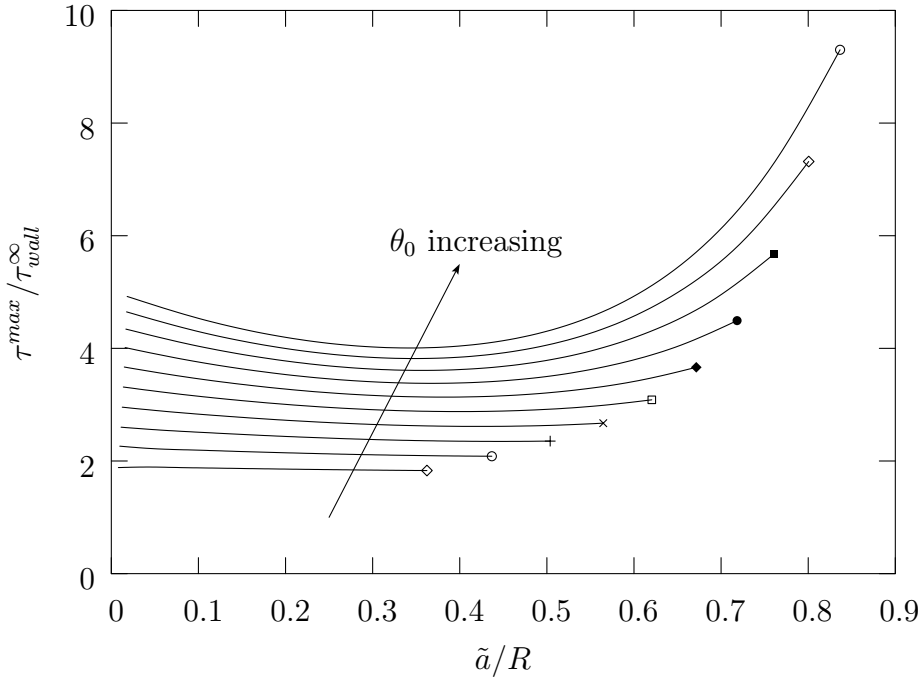

Figure 4.10: Maximum shear stress τ^{max} versus the characteristic length of the hump $\tilde{a}$. The contact angle θ_0 varies from 30° to 120° while the curves are plotted for every 10°.

expected to be similar to the results by modeling the large tube as a solid plane. Our results are in excellent agreement with the computations by Pozrikidis[23] for the shear stress on a three-dimensional protuberance on a solid plane under simple shear flow, as shown in figure 4.12. In addition, both studies agree on the fact that the maximum shear stress ratio $\tau^{max}/\tau^{\infty}_{wall} \approx 4.0$. Nevertheless, discrepancy still occurs on the surface of the cylinder near the hump. On the other hand, for a protuberance/cell having a comparable size with the radius of the cylindrical tube, i.e., $\tilde{a}/R \sim O(1)$, we have to establish a three-dimensional cylinder to accurately

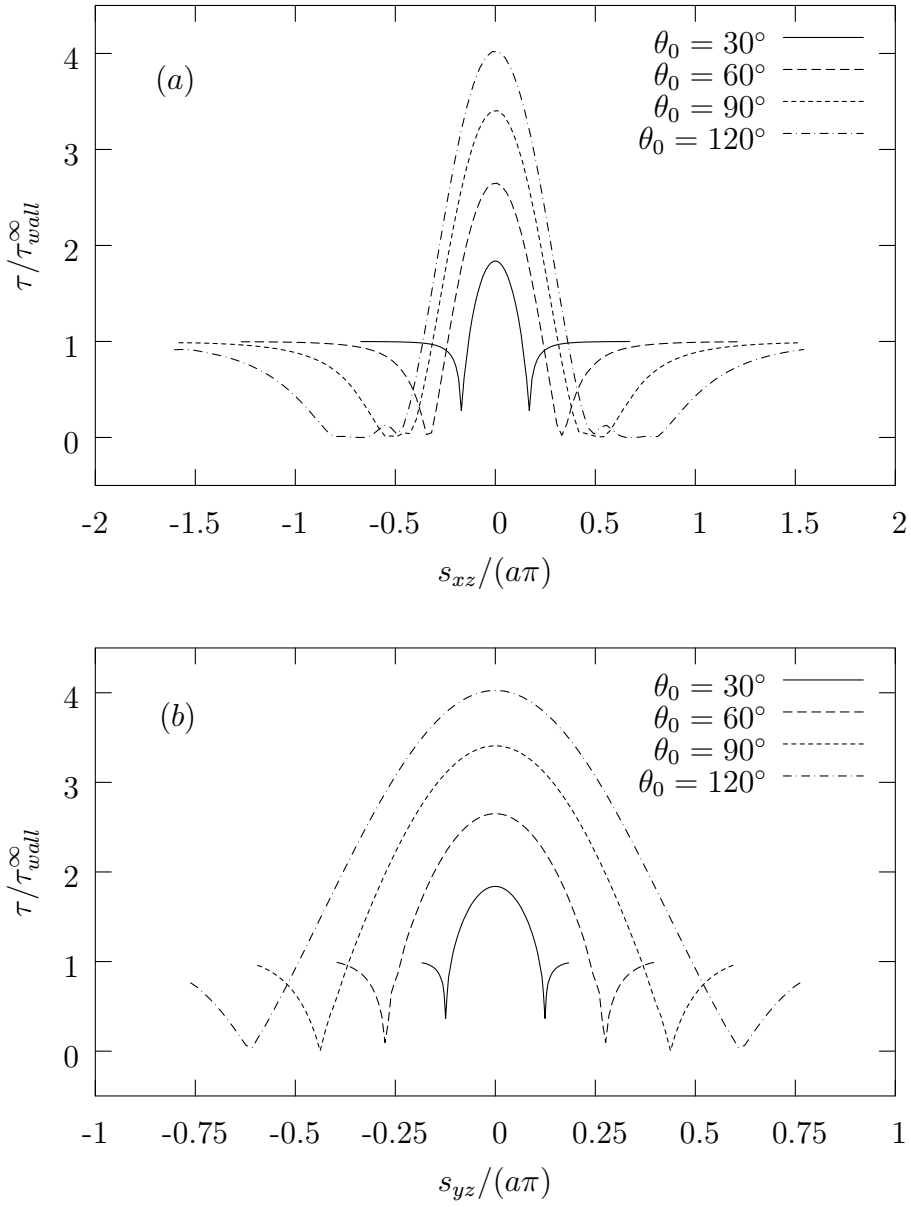

Figure 4.11: The influence of the contact angle θ_0 on the shear stress distribution on the hump. The shear stress τ is plotted as a function of the arc length s at the intersections of the hump surface with (a) the XZ plane and (b) the YZ plane. For both plots, the hump volume is $\tilde{a}/R = 0.30$, while the contact angle $\theta_0 = 30°$, $60°$, $90°$, $120°$.

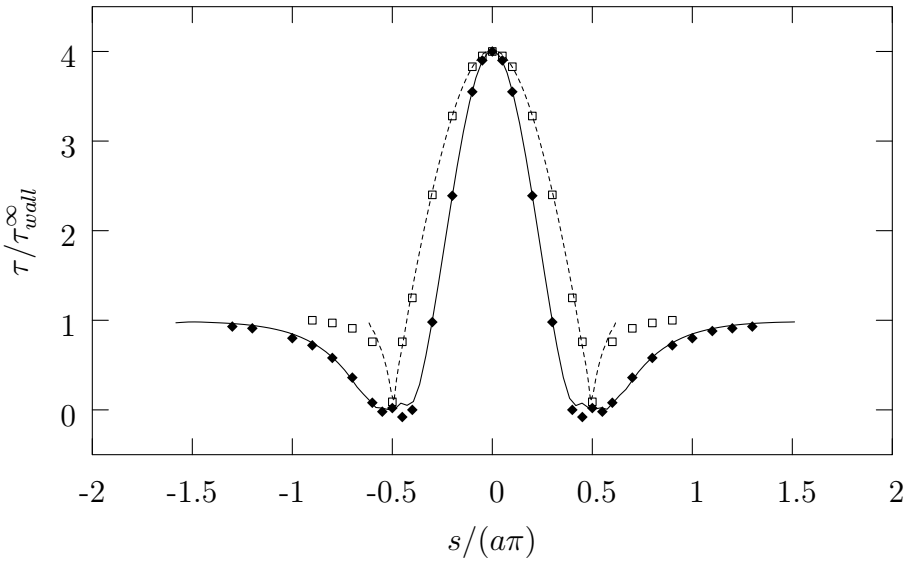

Figure 4.12: Comparison of the shear stress on the hump in a cylindrical tube with $\tilde{a}/R = 0.016$ and that on a plane. The solid curve describes the distribution of the shear stress τ on the hump in the cylindrical tube along the intersection of the hump surface with the XZ plane. The dashed curve represents the same quantity for the YZ plane. The solid diamonds and the open squares are the corresponding stress for the case of a hump on a plane taken from Ref.[23].

describe the stress exerted on the protuberance.

Finally, we investigate the total force and torque exerted on the hump by the tube flow. These two physical variables play a pivotal role in the cell adhesion process. The total force and torque are balanced by the receptor-ligand binding force on the surface of the cell[14]. Figure 4.13 and 4.14 demonstrate the magnitudes of the total force F_x and torque T_y exerted on the hump as functions of the characteristic length of the hump $\tilde{a}$ and the angle θ_0. For a constant hump volume V, both F_x

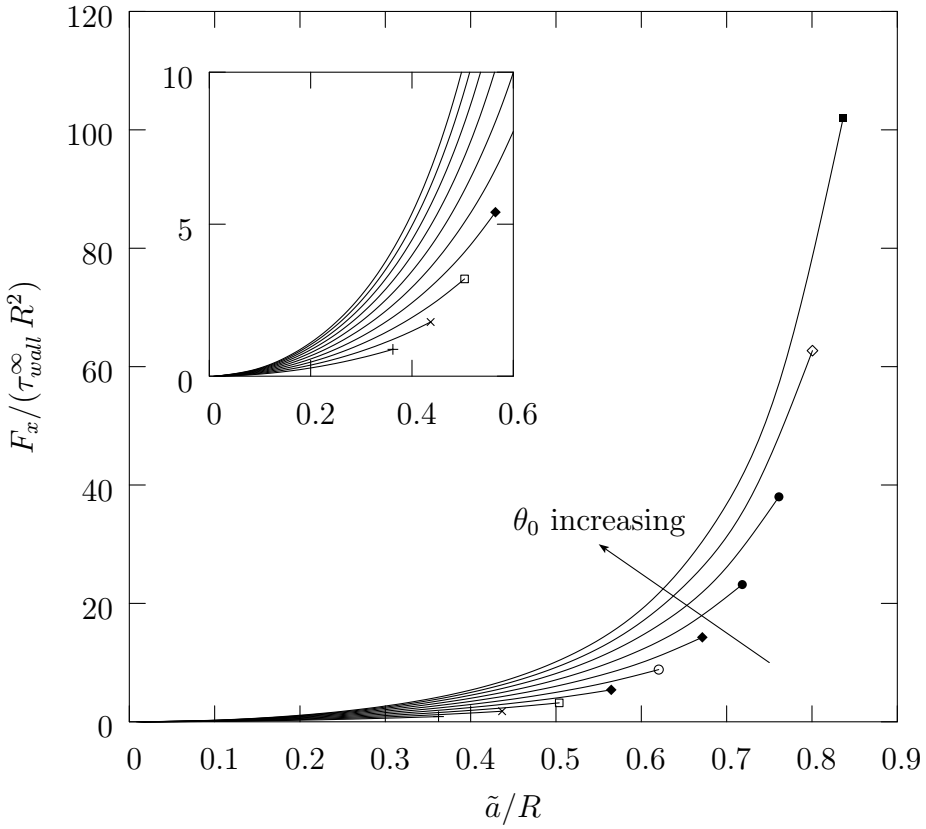

Figure 4.13: The total force F_x exerted on the hump versus the characteristic length of the hump $\tilde{a}$. The contact angle θ_0 varies from 30° to 120° while the curves are plotted for every 10°.

and T_y show a monotonic increase with the angle θ_0 due to the corresponding higher blocking. For a constant angle θ_0, both F_x and T_y demonstrate an increase with the hump volume V (i.e., the characteristic length $\tilde{a}$); the increase is more pronounced for large angles θ_0.

By comparing figure 4.13 with figure 4.10, we note that the maximum shear stress shows a minimum as the hump volume increases, while the total force F_x increases with the hump volume monotonically. As the volume V increases, the total force F_x experiences a more pronounced increase than the maximum shear

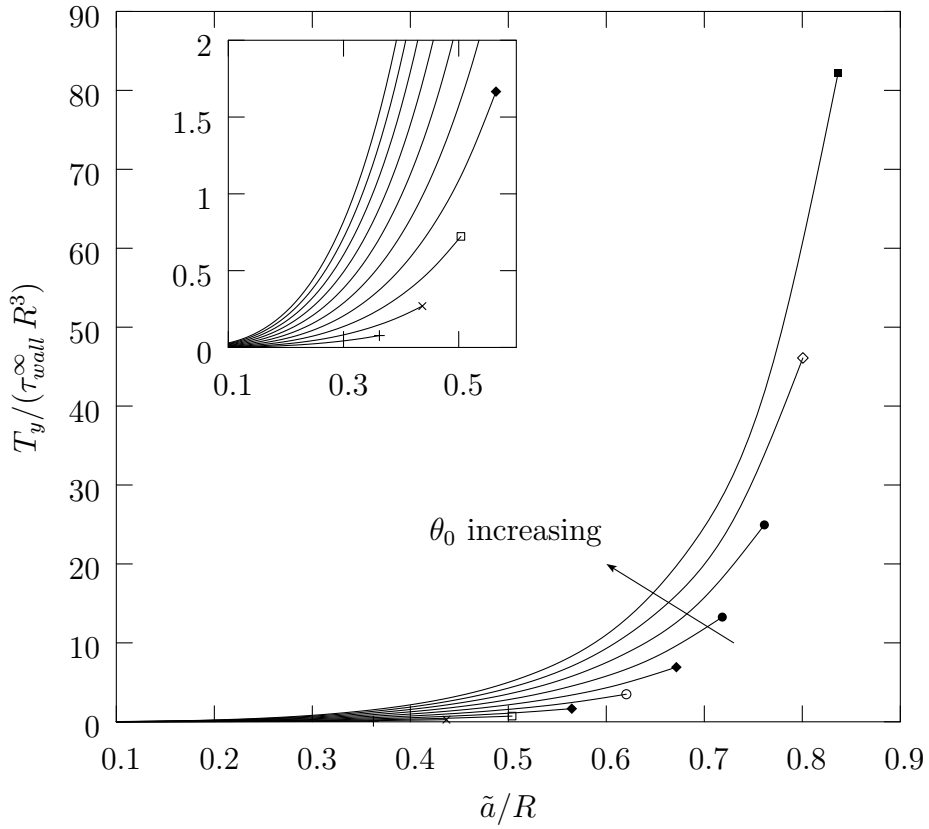

Figure 4.14: The torque T_y exerted on the hump versus the characteristic length of the hump $\tilde{a}$. The contact angle θ_0 varies from 30° to 120° while the curves are plotted for every 10°.

stress τ^{max}. To understand this phenomenon, we have to realize that the total force F_x has two components: the x-component of the shear stress τ^x and that of the normal force f_n^x. The x-component of the normal force f_n^x increases monotonically with the volume V as shown in figure 4.15 for a constant angle $\theta_0 = 90°$. Thus, the monotonic increase of F_x with the hump volume V results from the corresponding increase of f_n^x.

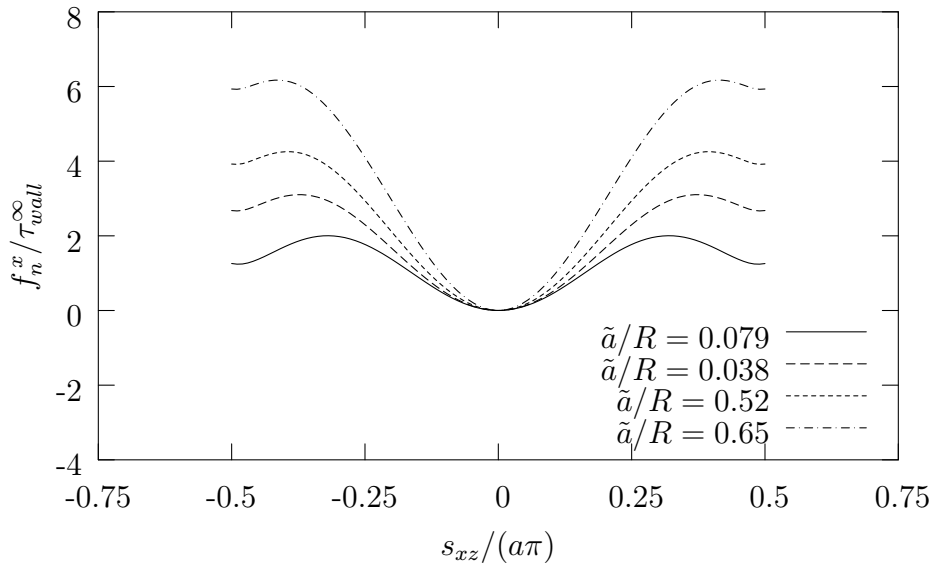

Figure 4.15: The x-component of the normal force f_n^x on the surface of a hump spreading axisymmetrically on the inner surface of a cylindrical tube. The normal force f_n^x is plotted as a function of the arc length s_{xz} at the intersection of the hump surface with the XZ plane. The contact angle $\theta_0 = 90°$. The values of $\tilde{a}/R$ shown correspond to $a/R = 0.1, 0.5, 0.7, 0.9$. The wall shear stress far from the hump is denoted as τ_{wall}^∞.

Bibliography

[1] I. B. Bazhlekov, P. D. Anderson and H. E. H. Meijer, Nonsingular boundary integral method for deformable drops in viscous flows. *Phys. Fluids* **16**(4), 1064–1081 (2004).

[2] J. D. Buckmaster and J. E. Flaherty, The bursting of two-dimensional drops in slow viscous flow. *J. Fluid Mech.* **60**, 625–639 (1973).

[3] S. B. Brooks and A. Tozeren, Flow past an array of cells that are adherent to the bottom plate of a flow channel. *Comp. Fluids* **25**(8), 741–757 (1996).

[4] V. Cristini, J. Blawzdziewicz and M. Loewenberg, An adaptive mesh algorithm for evolving surfaces: simulations of drop breakup and coalescence. *J. Comp. Phy.* **168**, 445–463 (2001).

[5] F. R. Cunhua and M. Loewenberg, A study of emulsion expansion by a boundary integral method. *Mechanics Research Communications* **30**, 639–649 (2003).

[6] P. Dimitrakopoulos, Computational studies of droplet displacement in stokes flow. MS thesis, University of Illinois (1996).

[7] P. Dimitrakopoulos and J. J. L. Higdon, Displacement of fluid droplets from solid surfaces in low-Reynolds-number shear flows. *J. Fluid Mech.* **336**, 351–378 (1997).

[8] P. Dimitrakopoulos and J. J. L. Higdon, On the displacement of three-dimensional fluid droplets from solid surface in low-Reynolds-number shear flows. *J. Fluid Mech.* **377**, 189–222 (1998).

[9] P. Dimitrakopoulos, Displacement of fluid droplets from solid surfaces. Ph.D. thesis, University of Illinois (1998).

[10] P. Dimitrakopoulos and J. J. L. Higdon, On the gravitational displacement of three-dimensional fluid droplets from inclined solid surfaces. *J. Fluid Mech.* **395**, 181–209 (1999).

[11] P. Dimitrakopoulos and J. J. L. Higdon, On the displacement of three-dimensional fluid droplets adhering to a plane wall in viscous pressure-driven flows. *J. Fluid Mech.* **435**, 327–350 (2001).

[12] P. Dimitrakopoulos and J. J. L. Higdon, On the displacement of fluid bridges from solid surfaces in viscous pressure-driven flows. *Phys. Fluids* **15**(10), 3255–3258 (2003).

[13] K. Feigl, S. F. M. Kaufmann, P. Fischer and E. J. Windhab, A numerical procedure for calculating droplet deformation in dispersing flows and experimental verification. *Chem. Eng. Sci.* **58**, 2351–2363 (2003).

[14] D. P. Gaver and S. Kute, A theoretical model study of the influence of fluid stresses on a cell adhering to a microchannel wall. *Biophys. J.* **75**, 721–733 (1998).

[15] S. Guido and M. Villone, Three-dimensional shape of a drop under simple shear flow. *J. Rheol.* **43**(2), 395–415 (1998).

[16] A. L. Hazel and T. J. Pedley, Vascular endothelial cells minimize the total force on their nuclei. *Biophys. J.* **78**, 47–54 (2000).

[17] J. J. L. Higdon, Stokes flow in arbitrary two-dimensional domains: shear flow over ridges and cavities. *J. Fluid Mech.* **159**, 195–226 (1985).

[18] J. J. L. Higdon and G. P. Muldowney, Resistance functions for spherical particles, droplets and bubbles in cylindrical tubes. *J. Fluid Mech.* **298**, 193–210 (1995).

[19] M. Loewenberg and E. J. Hinch, Numerical simulation of a concentrated emulsion in shear flow. *J. Fluid Mech.* **321**, 395–419 (1996).

[20] G. P. Muldowney and J. J. L. Higdon, A spectral boundary element approach to three-dimensional Stokes flow. *J. Fluid Mech.* **298**, 167-192 (1995).

[21] Y. Navot, Critical behavior of drop breakup in axisymmetric viscous flow. *Phys. Fluids* **11**(5), 990–996 (1999).

[22] C. Pozrikidis, *Boundary Integral and Singularity Methods for Linearized Viscous Flow.* Cambridge University Press, Cambridge (1999).

[23] C. Pozrikidis, Effect of pressure gradient on viscous shear flow past an axisymmetric depression or protuberance on a plane wall. *Comp. Fluids* **29**, 617–637 (2000).

[24] J. M. Rallison and A. Acrivos, A numerical study of the deformation and burst of a viscous drop in an extensional flow. *J. Fluid Mech.* **89**, 191–200 (1978).

[25] J. M. Rallison, A numerical study of the deformation and burst of a viscous drop in general shear flows. *J. Fluid Mech.* **109**, 465–482 (1981).

[26] J. M. Rallison, The deformation of small viscous drops and bubbles in shear flows. *J. Fluid Mech.* **16**, 45–66 (1984).

[27] N. Resnick, H. Yahav and A. Shay-Salit, Fluid shear stress and the vascular endothelium: for better and for worse. *Prog. Biophys. Molecular* **81**, 177–199 (2003).

[28] S. Richardson, Two-dimensional bubbles in slow viscous flows. *J. Fluid Mech.* **33**, 475–493 (1968).

[29] S. Richardson, Two-dimensional bubbles in slow viscous flows. Part 2. *J. Fluid Mech.* **58**, 115-127 (1973).

[30] J. Roumeliotis and G. R. Fulford, Droplet interactions in creeping flow. *Comp. Fluids* **29**, 435–450 (2000).

[31] H. A. Stone, Dynamics of drop deformation and breakup in viscous fluids. *Annu. Rev. Fluid Mech.* **26**, 65–102 (1994).

[32] M. Sugihara-Seki, Flow around cells adhered to a microvessel wall II: Comparison to flow around adherent cells in channel flow. *Biorheology* **38**, 3-13 (2001).

[33] M. Sugihara-Seki and G. W. Schmid-Schonbein, The fluid shear stress distribution on the membrane of leukocytes in the microcirculation. *Trans. ASME* **125**, 628–638 (2003).

[34] G. I. Taylor, The viscosity of a fluid containing small drops of another fluid. *Proc. Roy. Soc., A* **138**, 41–48 (1932).

[35] G. I. Taylor, The formation of emulsions in definable fields of flow. *Proc. Roy. Soc., A* **146**, 501–523 (1934).

[36] G. I. Taylor, Conical free surfaces and fluid interfaces. *Proc. 11th Int. Cong. Appl. Mech., Munich* (1964).

[37] G. K. Youngren and A. Acrivos, On the shape of a gas bubble in a viscous extensional flow. *J. Fluid Mech.* **76**, 433–442 (1976).

[38] A. Z. Zinchenko, M. A. Rother and R. H. Davis, A novel boundary-integral algorithm for viscous interaction of deformable drops. *Phys. Fluids* **9**(6), 1493–1511 (1997).